



Cleveland State University  
[EngagedScholarship@CSU](mailto:EngagedScholarship@CSU)

---

[ETD Archive](#)


---

Spring 5-3-2022

## Development And Analysis Of Next-Generation Polymeric And Bio-Ceramic Based Orthopedic Scaffolds By Advanced Manufacturing Techniques

Sudeep K. Gummadi

Follow this and additional works at: <https://engagedscholarship.csuohio.edu/etdarchive>

 Part of the [Biology Commons](#), and the [Molecular Biology Commons](#)

How does access to this work benefit you? Let us know!

---

DEVELOPMENT AND ANALYSIS OF NEXT-GENERATION POLYMERIC AND  
BIO-CERAMIC BASED ORTHOPEDIC SCAFFOLDS BY ADVANCED  
MANUFACTURING TECHNIQUES

SUDEEP KUMAR GUMMADI

Bachelor of Technology in Mechanical Engineering

Sreenidhi Institute of Science and Technology

August 2019

Submitted in partial fulfillment of requirements for the degree

Master of Science in Mechanical Engineering

at the

CLEVELAND STATE UNIVERSITY

May 2022

We hereby approve this thesis for

SUDEEP KUMAR GUMMADI

Candidate for the Master of Science in Engineering degree for the

Department of Mechanical Engineering

and the CLEVELAND STATE UNIVERSITY'S

College of Graduate Studies by

---

Committee Chairperson, Dr. Prabaha Sikder

---

Department of Mechanical Engineering

---

Committee Member, Dr. Tushar Borkar

---

Department of Mechanical Engineering

---

Committee Member, Dr. Saeed Farahani

---

Department of Mechanical Engineering

Student's Date of Defense: 05/03/2022

## ACKNOWLEDGMENT

First and foremost, I would like to thank my research advisor Dr. Prabaha Sikder for guiding me in this research project as well as academics during my master's program. His support and knowledge made it possible for me to present this work. I learned so much from him both professionally and personally and has helped and supported me tremendously.

I would also like to sincerely acknowledge Dr Tushar Borkar for providing me the facility of his lab equipment especially Spark Plasma Sintering. I'm sincerely thankful to Amit Patil for helping me sinter the samples and for teaching me Scanning Electron Microscopy in this Research. I'm also very thankful to my lab mates Bharath Tej Challa and Laura Juliana Azuero for constant support.

I would like to express my gratitude to Dr. Tushar Borkar and Dr. Saeed Farahani who are agreed to be part of my thesis committee.

I'm forever grateful to my parents for all the encouragement and support they gave me and finally I'm very thankful to my friends who stood for me constantly irrespective of the situation and made me achieve this.

This work is supported by Dr. Sikder's STARTUP and FRD grant at Cleveland State University and NSF I-corps grant.

DEVELOPMENT AND ANALYSIS OF NEXT-GENERATION POLYMERIC AND  
BIO-CERAMIC BASED ORTHOPEDIC SCAFFOLDS BY ADVANCED  
MANUFACTURING TECHNIQUES

SUDEEP KUMAR GUMMADI

**ABSTRACT**

3D printing, specifically Fused Deposition Modelling (FDM) of Poly-ether-ether-ketone (PEEK), was used to develop design-specific PEEK structures. In this study, we investigate the effect of specific 3D printing parameters such as nozzle and chamber temperature, print speed, and layer height on the mechanical properties of 3D printed PEEK. Moreover, we explored the effect of filament quality on the mechanical properties of the PEEK structures. In that regard, we developed PEEK filaments using a customized extruder setup in-house and used those laboratory-developed filaments (LD) to 3D print PEEK structures suitable for mechanical testing and compared them to the mechanical properties of 3D printed parts that were developed using commercially available (CA) filaments. Notably, results confirmed no significant differences but highlighting that the LD filaments were of comparable quality to the CA ones.

Polyether-ether-ketone (PEEK) is a high strength semi crystalline thermoplastic and is one of the most common materials used for orthopedic devices. It is a promising biomaterial that could potentially replace metal and ceramic-based medical devices owing to its good mechanical properties and biocompatibility. However, the poor osseointegration property of PEEK implants have limited its' clinical applications. To address this issue, in this study, we developed PEEK scaffolds with controlled pore sizes. We hypothesize that the porous PEEK will help in efficient osseointegration while not compromising the

mechanical properties of the scaffolds. PEEK scaffolds with controlled and designed pore sizes of 0.3mm, 0.4mm, 0.6mm, 0.8mm and 1mm will be manufactured via FDM.

Amorphous Magnesium Phosphates (AMP) is one of the less explored bio ceramics which has good potential in bone regeneration. However, its application is limited by its poor mechanical properties such as brittleness. To address this issue, Graphene Nanoplatelets will be incorporated in AMP using ball milling approach (dry ball milling), followed by consolidation using spark plasma sintering (SPS) technique. Post sintering, the mechanical, material, corrosion, and in vitro biological properties of the AMP-GNP composites will be analyzed in detail. The hypothesis of this project is that the GNP incorporation in AMP will enhance AMP's mechanical properties, decrease its corrosion behavior and in addition do not affect the biological properties of the specimens.

## TABLE OF CONTENTS

	Page
ABSTRACT.....	xiii
LIST OF TABLES .....	xviii
LIST OF FIGURES .....	xix
CHAPTER	
I In-House Processing of 3-D Printable Poly-Ether-Ether-Ketone (PEEK) Filaments and the Effect of Fused Deposition Modelling Parameters on 3D Printed PEEK Structures.....	1
1.1 Introduction.....	1
1.2 Experimental.....	5
1.2.1 Raw Materials for 3D Printing.....	5
1.2.2 In-House Feedstock Filament Extrusion.....	6
1.2.3 Physical and Thermal Characterization .....	7
1.2.4 FDM-3D Printing Parameters .....	8
1.2.5 Mechanical Properties.....	8
1.2.6 Statistical Analysis.....	9
1.3 Results.....	10
1.3.1 Compressive Strengths.....	10
1.3.2 Tensile Strengths.....	13
1.3.3 Flexural Strengths .....	14
1.4 Discussion.....	16
1.5 Conclusion .....	25

II	Mechanical Properties of 3D Printed Porous PEEK Orthopedic Scaffolds.....	26
	2.1 Introduction.....	26
	2.2 Materials and Methods.....	30
	2.2.1 Raw Materials for 3D Printing.....	30
	2.2.2 FDM-3D Printing Parameters.....	30
	2.2.3 Physical Characterization.....	32
	2.2.4 Finite Element Analysis.....	32
	2.2.5 Statistical Analysis.....	33
	2.3 Results and Discussion.....	33
	2.3.1 Porous Scaffold Morphology.....	33
	2.3.2 Mechanical Properties.....	37
	2.3.3 Finite Element Analysis.....	41
	2.3.3.1 Yield Compressive Strength.....	42
	2.3.3.2 Stress Distribution Analysis.....	44
	2.3.3.3 Buckling Nature.....	47
	2.4 Conclusion.....	51
III	Spark Plasma Sintering of Strengthened Amorphous Magnesium Phosphate-Graphene Nano Platelet (AMP-GNP) Bio-Composites for Orthopedic Implants.....	53
	3.1 Introduction.....	53
	3.2 Materials and Methods.....	57
	3.2.1 Raw Material.....	57
	3.2.2 Dry Ball Milling of the AMP-GNP Composites.....	57



3.2.3 Spark Plasma Sintering (SPS) of the Nanocomposites .....	58
3.2.4 Polishing .....	58
3.2.5 Structural Characterization .....	58
3.2.6 SBF Immersion Studies .....	59
3.2.7 Mechanical Property Characterization.....	59
3.3 Results and Discussion .....	60
3.3.1 Physical Characterization.....	60
3.3.2 SBF Immersion Studies .....	64
3.3.3 Mechanical Property Analysis .....	67
3.4 Conclusion .....	68
REFERENCES .....	69

## LIST OF TABLES

Table	Page
1.1 The variable and fixed 3D printing parameters followed in this study.....	8
2.1 FDM Parameters used for printing the PEEK Scaffolds. ....	31
2.2 Abaqus isotropic, elasto-plastic model parameters.....	33
2.3 Pore Size Distribution of the 3D printed porous scaffolds. ....	36
2.4 Compression strength of the porous PEEK specimens from FEA simulations with constant Young's Modulus=3000 MPa. ....	43
2.5 Compression strength of the porous PEEK specimens from FEA simulations with variable Young's Modulus.....	44
2.6 Buckling Loads of the porous PEEK specimens from FEA simulations with constant Young's Modulus=688 MPa.....	50
2.7 Buckling Loads of the porous PEEK specimens from FEA simulations with variable Young's Modulus.....	50

## LIST OF FIGURES

Figure	Page
1.1 Photograph of the entire laboratory extruder setup that was used to develop the PEEK filaments .....	7
1.2 CAD diagrams and corresponding 3D models .....	10
1.3 Photographs of 3D printed PEEK specimens developed by LD filaments.....	12
1.4 Comparison of compressive strengths of specimens .....	12
1.5 Comparison of tensile strengths of specimens .....	14
1.6 Comparison of flexural strengths of specimens .....	16
1.7 SEM image showing the cross-section of a LD PEEK filament .....	17
1.8 Photograph of the topmost layer of a 3D printed compression PEEK specimen. ....	18
1.9 Effect of annealing on 3D printed PEEK.....	20
1.10 Photograph of a femoral head.....	25
2.1 Stereomicroscopy and corresponding Scanning Electron Microscopy (SEM) images .....	36
2.2 Stress-Strain Curves of porous PEEK specimens.....	41
2.3 Yield compressive strength and Young's Modulus of porous PEEK specimens with different pore sizes .....	41
2.4 3D rendered images of the scaffolds as designed in Solidworks.....	41
2.5 Finite Element Analysis results of the PEEK porous specimens.....	46
2.6 Failure modes of the 3D printed PEEK specimens.....	48
3.1 Digital photographs of the pristine AMP and AMP with varying GNP .....	60

3.2	Digital photographs of the sintered i.e., SPS-ed AMP and AMP with varying GNP .....	61
3.3	X-ray diffraction of the nanocomposite powders .....	62
3.4	Back scattered-Scanning electron microscopy (BS-SEM) analysis of the SPS-ed AMP and AMP-GNP specimens.....	63
3.5	High magnification SEM image (secondary electron detector) showing the porous structure on the top surface of a sintered AMP scaffold.....	63
3.6	SEM images of the specimen surface after SBF immersion for 7 days.....	65
3.7	EDS analysis of SBF immersed specimens .....	66
3.8	Weight gain analysis of the specimens after immersing in SBF for 7 days .....	67
3.9	Hardness test.....	68

## CHAPTER I

### In-House Processing of 3-D Printable Poly-Ether-Ether-Ketone (PEEK) Filaments and the Effect of Fused Deposition Modelling Parameters on 3D Printed PEEK Structures

#### 1.1 Introduction

Poly-ether-ether-ketone (PEEK,  $(-C_6H_4-OC_6H_4-O-C_6H_4-CO-)_n$ ) is a semicrystalline, thermoplastic polymer belonging to the poly-aryl-ether-ketone (PAEK) family[1]. As opposed to some well-known polymer counterparts like Polylactic acid (PLA), Polycaprolactone (PCL), and Acrylonitrile Butadiene Styrene (ABS), PEEK exhibits outstandingly high mechanical properties and melting temperature. It has Young's modulus of around 4 GPa, tensile strength around 145 MPa, and a melting point at 343°C[1]. PEEK is also highly resistant to thermal and chemical degradation. These high-quality properties make PEEK one of the most suitable advanced polymers used in a wide variety of high-performance applications in aerospace, automotive, military, oil and gas, and chemical industries [2]. In addition, PEEK is a preferred biomaterial to make craniofacial, maxillofacial, orthopedic, and spinal implants because of its biocompatibility, radiolucency, chemical stability inside the body, and a close match to the mechanical properties of bone [3][4, 5].

Traditionally, PEEK products are processed by conventional methods such as injection molding, compression molding, or machining extruded PEEK rods. However, these methods require multiple processing steps, lack the capability to make complex-designed products, and involve high chances of dimensional inaccuracies and contamination from machining tools in the final part. Hence, when Additive Manufacturing (AM), better known as 3-dimensional or 3D printing came into the industry and started developing components by a top-down or bottom-up layer-by-layer approach, it eliminated the shortcomings of conventional manufacturing techniques and allowed developers to make PEEK parts of any complex design with utmost precision easily [6].

At first, 3D printing of PEEK was only limited to the Selective Laser Sintering (SLS) technique because SLS is the only 3D printing technique that involves high processing temperature ranges, ones which can accommodate PEEK printing [7]. However, the SLS apparatus is highly sophisticated, involves multiple complicated and expensive components, and requires skilled operators. Also, the starting material needs to be in the form of powder, and SLS processing of PEEK is complicated by its varying particle morphology and size distribution, and the un-sintered powder goes waste [7], [8]. These shortcomings restricted the expansive and broad-ranging development of 3D-printed PEEK products to some extent.

On the other hand, Fused Deposition Modelling (FDM) is the most well-known and widely used 3D printing technique with many advantages, including low cost, minimal waste, and simplicity in which it can be installed on benchtops and it is easy to operate compared to other AM techniques [9]. Also, it is convenient to develop polymer composites compatible with FDM printers [10] [11] [12]. However, FDM of PEEK is

complex and requires careful processing, especially when the aim is to print products that exhibit mechanical properties close to those developed in conventional manufacturing techniques such as injection molding. FDM of PEEK requires high thermal processing parameters such as nozzle, bedplate, and chamber temperatures. It is also well known that FDM-developed (FDM-d) PEEK parts are prone to warping, involve high thermal stress, and are prone to poor interlayer adhesion [13]. Since 2014, various research groups have explored FDM of PEEK using customized 3D printers and feedstock filaments. Valentan et al.[14] and Wu et al.[15] were some of the firsts to establish a particular FDM 3D printer that could achieve the required nozzle and chamber temperatures to process PEEK material. Subsequently, other research groups explored the effect of various FDM-specific parameters on the material and mechanical properties of 3D printed PEEK products. In a critical study, Wu et al.[16] investigated the influence of layer thickness and raster angle on the mechanical properties of FDM-d PEEK and further compared the properties with PEEK parts made by injection molding. The study concluded that optimal mechanical properties of PEEK could be observed in samples with 0.3 mm layer thickness and a raster angle of  $0^{\circ}/90^{\circ}$ , but the properties of 3D printed PEEK parts were significantly lower than those developed by injection molding. Vaezi and Yang [17] performed a detailed exploration of various thermal parameters on the quality of PEEK parts. The authors observed that nozzle temperatures within the range of 400–430 $^{\circ}$ C was suitable for 3D printing PEEK. Further, they also indicated that a chamber temperature of 80 $^{\circ}$ C and a heated build plate at 130 $^{\circ}$ C are critical to assure a suitable PEEK/substrate and PEEK interlayer bonding, avoid warpage, minimize delamination, and reduce polymer degradation. Yang et al.[18] analyzed the effect of various thermal conditions on PEEK

parts and observed that a high chamber temperature (150<sup>0</sup>C and 200<sup>0</sup>C) and annealing can significantly enhance the crystallinity of PEEK and hence improve the mechanical properties of the printed parts.

In the last few years, many researchers have conducted in-depth studies to analyze the effect of various kinds of FDM processing parameters on PEEK properties [19],[20]. We also thoroughly explored the effect of FDM parameters on the mechanical properties of 3D printed PEEK structures [21]. Yet, it should also be noted that apart from FDM processing parameters, the quality of the feedstock filaments also play a significant role in the mechanical properties of the filament. Deviations in the diameter of the feedstock filament can cause material deficit or surplus in layers [14] and air gaps between adjacent filaments in the printed parts [17], leading to mechanical property degradation. Through a series of experiments, Zhao et al.[22] confirmed that the diameter deviation of the feedstock filament was a critical factor in influencing the quality of the printed parts. Lesser variations lead to fewer voids in the printed parts, thus enhancing mechanical property. Many research groups that focused on the FDM of PEEK developed their in-house 3-D printable PEEK filaments, but very few considered the effect of feedstock filament quality. Indeed, it is challenging to form constant diameter PEEK filaments primarily because of the high extrusion temperatures and viscosity of PEEK. In the recent 2-3 years, there has been a surge in the research and development of FDM-d PEEK, because of the availability of various cost-effective, high-temperature 3D printers. Moreover, companies like Invibio, Apium, and 3DXTECH have become well-known 3D printable PEEK filament manufacturers. However, it does not give innovators the chance to develop 3D printable filaments of customized compositions, for instance, PEEK-based composites [23].



In this study, we developed an extrusion setup and used it to form constant-diameter PEEK filaments. Subsequently, the filaments were used in a high-temperature FDM printer to print various PEEK specimens for mechanical testing. We aimed to compare the quality of the laboratory-developed (LD) filaments to one of the most well-known commercially available (CA) filaments. Therefore, we performed a thorough comparative analysis between the tensile, compressive, and flexural strengths of the 3D printed specimens developed from LD and CA filaments. Further, we explored the effects of crucial 3D printing parameters like nozzle and chamber temperature, print speed, and layer height on the mechanical properties of specimens developed from both CA and LD filaments. We expect this study to provide the necessary guidance to researchers and developers about choosing LD or CA filaments and combining them with an optimized set of printing parameters to achieve high-quality FDM-d PEEK parts.

## **1.2 Experimental**

### **1.2.1 Raw Materials for 3D Printing**

For the LD 3D printable filaments, PEEK 450G Type Unfilled Natural Pellets (Filastruder, Snellville, GA, USA) was used. The filament extruder and filament winder parts were procured from Filastruder and assembled in-house. A 15V, 150W power supply (LRS-150F-15, Mean Well, New Taipei City, Taiwan) was used for increasing the extruder temperature up to 450<sup>0</sup>C and a 1" thick Ceramic Fiber Insulation Kao wool insulation blanket (Lynn Manufacturing Inc, Lynn, MA, USA) was wrapped around the extruder barrel to maintain the high extrusion temperature. The CA filament used in this study was Thermax<sup>TM</sup> PEEK Natural (3DXTECH, Grand Rapids, MI, USA) filament with a diameter of 1.75 mm.

### 1.2.2 In-House Feedstock Filament Extrusion

3D printable LD PEEK filament was made by a customized device assembly comprising of **1)** a single-screw extruder, **2)** a sensor controlling the speed of filament winding, and **3)** a filament winding setup as shown in **Figure 1.1**. All the parts were procured from Filastruder. **Figure 1.1** also shows the entire extrusion and filament spooling setup. The PEEK pellets were first dried at 120<sup>0</sup>C for 5h in a convection oven and fed to a single-screw extruder with the help of a custom-designed hopper. The single screw extruder (with a Ø1.6 mm nozzle) was kept at a raised angular position with respect to the sensor and the winder setup. The extruder screw (length = 150 mm) speed was set at 10 rpm, and the temperature was maintained at 355<sup>0</sup>C throughout. We didn't use any additional quenching step apart from ambient atmosphere cooling as it affected the uniformity in the filament dimension. Once a filament was extruded out, it was guided through a sensor that detects the filament's position and adjusts the speed of the winder. The filament was then guided through a loop of polytetrafluoroethylene (PTFE) tube that provides tension (and stretch) to resist tangles. Once the filament left the PTFE tube, a filament guide evenly spread the filament across the spool to avoid bundling up at only one region. Depending on the positioning of the filament on the spool, the filament winding setup automatically adjusted the speed of spool rotation to induce a favorable tension to the ongoing extruded filaments. After an entire spool of PEEK filament was formed, it was stored at 120<sup>0</sup>C until further usage.

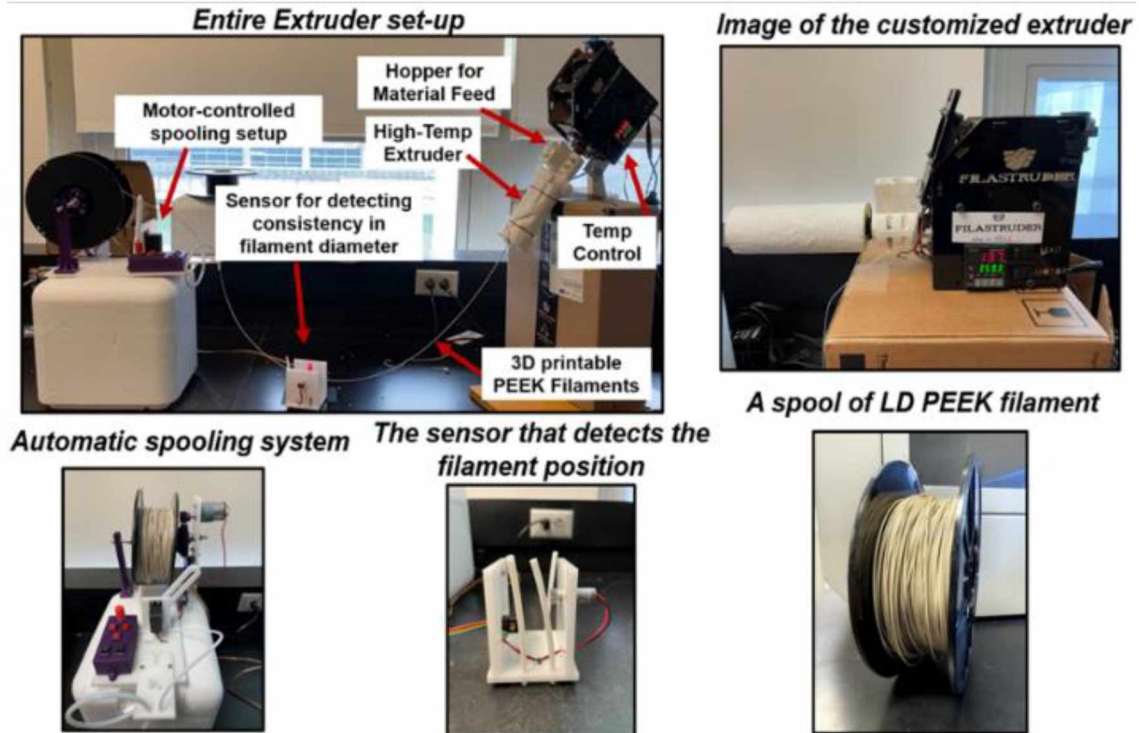


**Figure 1.1:** Photograph of the entire laboratory extruder setup that was used to develop the PEEK filaments. The major components that assemble to make the setup are the high temperature extruder, sensor that detects the filament position and an automatic guided spooling system.

### 1.2.3 Physical and Thermal Characterization

To analyze the extent of pores present in the filaments, both LD and CA filaments were cryo-fractured at three random locations along the filament spool length and analyzed using Scanning electron microscopy (SEM). The thermal properties of annealed and non-annealed specimens were investigated using Differential Scanning Calorimetry (DSC) (DSC 250, TA instruments, New Castle DE, USA). The degree of crystallinity ( $X_{cw}\%$ ) was calculated using the following equation

$$X_{cw}(\%) = \frac{H_m}{w_f \times H_c} \times 100\%$$

Where  $H_m$  is the melt enthalpy as obtained from the DSC scan,  $w_f$  is the weight fraction of PEEK (1), and  $H_c$  is the melt enthalpy of 100% crystalline PEEK (130 J.g<sup>-1</sup>).

#### 1.2.4 FDM-3D Printing Parameters

Both CA and LD PEEK filaments were dried at 120°C for 5h before using them for 3D printing. We used a FUNMAT HT Enhanced (Intamsys Technology Ltd., Shanghai, China) for 3D printing various PEEK specimens. We varied four different FDM parameters one at a time, keeping the others fixed, as shown in **Table 1.1**. For all the samples, the raster direction was an oblique direction of 45°, and the infill rate was 100%. The protocol of post-heat treatment (annealing) procedure for one set of samples was: 160 °C for 30 min, followed by 200 °C for 2 h, and gradual cooling to room temperature.

**Table 1.1:** The variable and fixed 3D printing parameters followed in this study.

<i>Variable Parameter</i>	<i>Nozzle Temp (°C)</i>	<i>Bed Plate Temp (°C)</i>	<i>Chamber Temp (°C)</i>	<i>Layer Height (mm)</i>	<i>Print Speed (mm/sec)</i>
<i>Nozzle Temp</i>	380	130	90	0.2	50
	400				
	410				
<i>Chamber Temp</i>	400	130	25	0.2	50
			90		
<i>Layer Height</i>	400	130	90	0.3	50
				0.2	
				0.1	
<i>Print Speed</i>	400	130	90	0.2	30
					40
					50

#### 1.2.5 Mechanical Properties

Tensile, compression, and flexural tests were performed on various 3D printed PEEK parts at room temperature. The Instron 3369 Universal Testing Machine (UTM) with a 50kN load cell and specific testing fixtures was used for the different mechanical tests. Compression testing was performed following ASTM D695 with a constant

displacement of 1.27 mm/min [24]. The dimensions of the cylindrical specimens are shown in **Figure 1.2a**. Tensile testing was performed following ISO 527-2 [25]. The CAD diagrams and 3D models (STL format) of the dog bone-shaped specimen dimensions are shown in **Figure 1.2b**. A fixed-gauge length 2630 series clip-on extensometer was clipped directly onto the specimen at the beginning of each tensile test. In addition, 5 mm/min strain deformation was used to measure the specimens' tensile strength. A 1kN load cell was used for the flexural tests, and ISO 178 was followed. The rectangular specimen dimensions are shown in **Figure 1.2c**. Flexural strength was calculated using the following equation.

$$\sigma = \frac{3PL}{2bt^2}$$

where:

$\sigma$  = Flexural Stress (MPa)

$P$  = Load (N)

$L$  = Support span (50 mm)

$b$  = width of specimen (mm)

$t$  = thickness of beam (mm)

### **1.2.6 Statistical Analysis**

All the tests were performed with a sample size  $n=4$ . One-way analysis of variance with Tukey test was conducted to determine the statistical difference between different specimen groups and  $p < 0.05$  were considered significant.

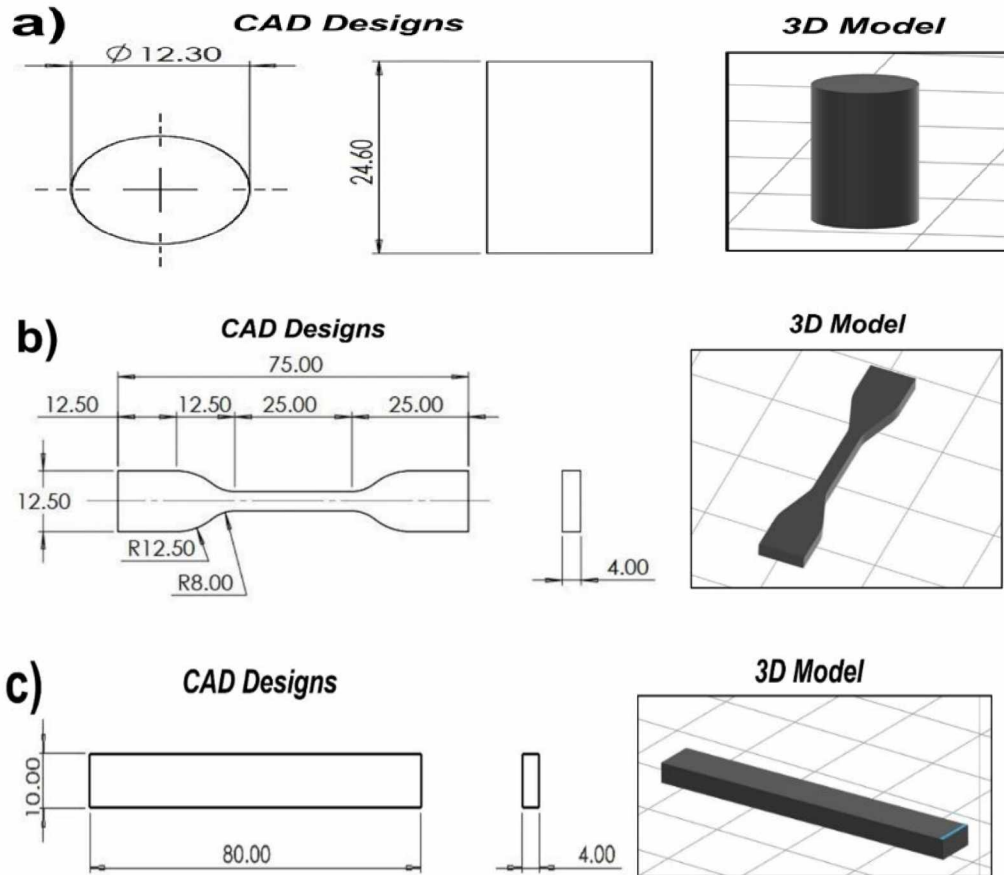


**Figure 1.2:** CAD diagrams and corresponding 3D models (as obtained from the slicing software) of the (a) compression, (b) tensile and (c) flexural test specimens.

## 1.3 Results

### 1.3.1 Compressive Strengths

The photograph of a cylinder-shaped compression testing specimen is shown in **Figure 1.3a**. The part exhibits a gradient of dark brown and light beige-colored regions all over the surface. While certain print layers and regions show prominent dark brown color, some regions show beige color. **Figure 1.4(a-d)** shows the compressive strengths of the specimens developed with LD and CA filaments as a function of various 3D printing parameters such as nozzle temperature, chamber temperature, printing speed, and layer height. Some critical observations can be made from the graphs – **First**, in all the cases of

varied printing parameters, the specimens developed with CA filaments exhibited moderately better compressive strengths than those produced with LD filaments. **Second**, higher nozzle temperature helps to enhance the compressive strengths of the 3D printed parts significantly. The highest compressive strength can be observed in the specimens printed at 410<sup>0</sup>C nozzle temperature using CA filaments (106.34 MPa); nonetheless, the parts printed at the same nozzle temperature using LD filaments exhibited a compressive strength of 104.76 MPa. **Third**, chamber temperature plays a significant role in improving the compressive strength of the specimens. In the case of the CA filaments, we noticed significantly higher compressive strengths of the samples printed at 90<sup>0</sup>C (107.69 MPa) compared to those printed at 25<sup>0</sup>C (91.24 MPa). The observations were the same for the parts printed with LD filaments; an increase of 16.5% was observed in the compressive strengths of the parts printed at 90<sup>0</sup>C (102.76 MPa) over those printed at 25<sup>0</sup>C (88.23 MPa). **Fourth**, increasing print speed steadily augments the compressive strengths of the parts printed with both LD and CA filaments. However, there were no significant differences in the compressive strengths of the parts printed at 50 mm/sec compared to those printed at 30 mm/sec. **Finally**, lowering the layer height thickness increases the compressive strengths of the specimens. Notably, a significant difference in the strengths can be noted between the samples printed with layer heights of 0.3 mm (89.23 MPa for LD filaments and 91.54 MPa for CA filaments) and 0.1 mm (107.45 MPa for LD filaments and 109.69 MPa for CA filaments).

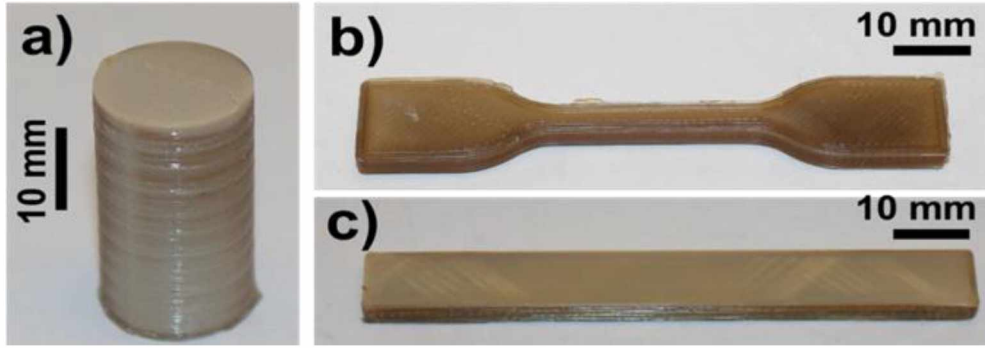


**Figure 1.3:** Photographs of 3D printed PEEK specimens developed by LD filaments for (a) compression, (b) tensile and (c) flexural tests

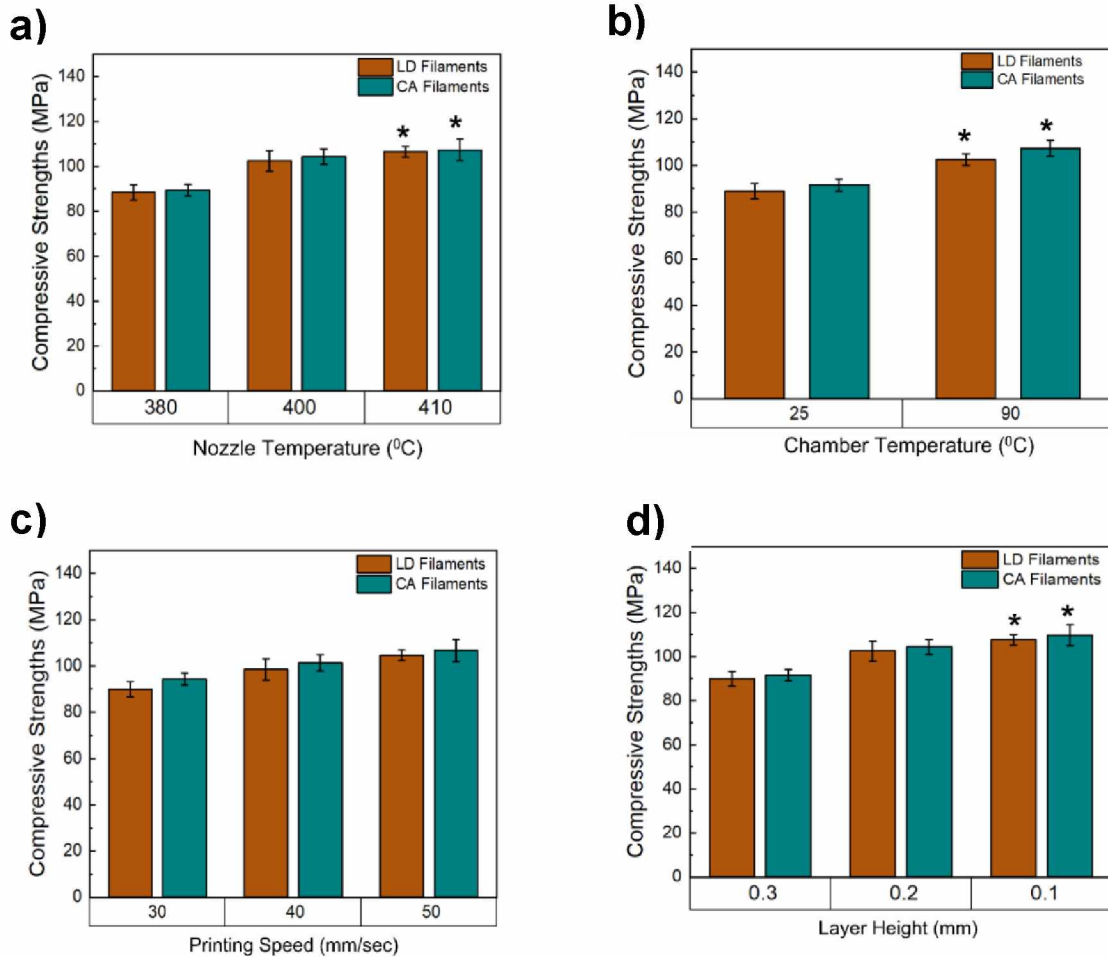


**Figure 1.4:** Comparison of compressive strengths of specimens developed by commercially available (CA) and laboratory developed (LD) filaments as a function of (a) printing speed (b) layer height, and (c) nozzle temperature. \* means that value is statistically significant with the values at 380°C, 25°C and 0.3 mm.



### 1.3.2 Tensile Strengths

The photograph of a 3D printed PEEK tensile specimen is shown in **Figure 1.3b**. Similar to the compression specimens, a dark brown and beige gradient can be observed all over the printed part. However, as opposed to the compression specimen, the color gradient was more prominent on the top surface of the printed part and not along with the layers, i.e., the part thickness. The deep brown color was evident along with the thickness of the tensile bar. **Figure 1.5(a-d)** shows the tensile strengths of the specimens printed with LD and CA filaments as a function of various 3D printing parameters. The graphs indicate some essential observations. **First**, like the compressive strengths, specimens printed with CA filaments exhibited better tensile strengths than the ones printed with LD filaments. In the majority of the cases, the differences were not significant, except for the two conditions. At 25<sup>0</sup>C, the specimens printed with LD filaments exhibited considerably lower tensile strength values (78.64 MPa) than those printed with CA filaments (89.24 MPa). Similarly, with 0.3 mm layer height, the tensile strengths of the parts printed with LD filaments were significantly lower (15.27%) than those printed with CA filaments. **Second**, higher nozzle temperature helps in a significant increase in the tensile strength of the specimens. Notably, the samples printed at 410<sup>0</sup>C and LD filament exhibited a mean tensile strength of 101.56 MPa. In addition, the rise in chamber temperature (90<sup>0</sup>C) significantly increases the tensile strength of the samples; in the case of LD filaments, the rise was 23.4%, and in the case of CA filaments, the rise was 19.2%. **Third**, lowering the print speed helped decrease the tensile strength, whereas reducing the layer height thickness increased the tensile strength. Interestingly, as opposed to the significant differences in tensile strengths between the parts printed with LD and CA filaments and 0.3 mm layer height, the parts printed with 0.1 mm

layer and LD filaments exhibited comparable tensile strengths (104.45 MPa) to the ones printed with CA filaments.

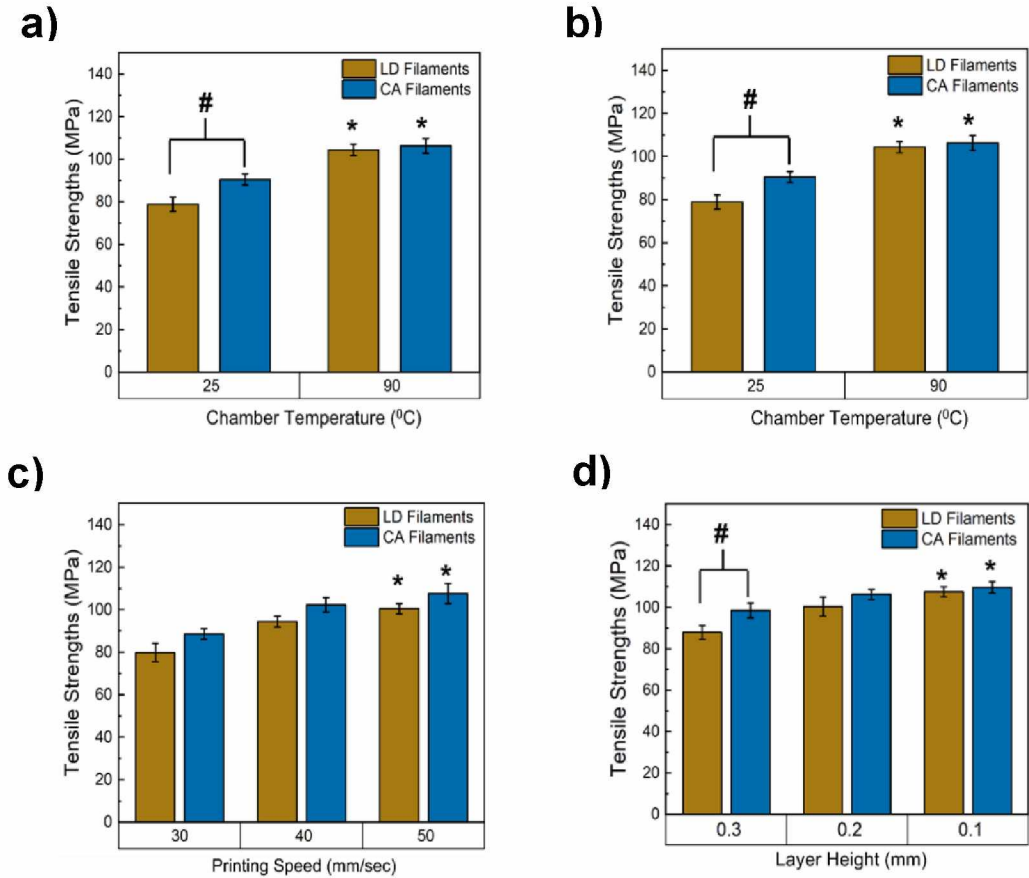


**Figure 1.5:** Comparison of tensile strengths of specimens developed by commercially available (CA) and laboratory developed (LD) filaments as a function of (a) printing speed (b) layer height, and (c) nozzle temperature. \* means that value is statistically significant with the values at 3800C, 250C, 30 mm/sec, and 0.3 mm. # means statistically significant between LA and CA filaments within the same 3D printing condition.

### 1.3.3 Flexural Strengths

A 3D printed PEEK specimen for flexural testing is shown in **Figure 1.3c**. Similar to the tensile test specimens, a dark brown and beige gradient can be seen on the specimen's top surface. Also, the dark brown color was predominant along with the thickness of the specimen. **Figure 1.6(a-d)** shows the flexural strength of the specimens printed with LD

and CA filaments as a function of Some important observations that can be made from the graphs are mentioned in the following. **First**, at every condition, the flexural strengths of the specimens printed with CA filaments were moderately better than those printed with LD filaments. No significant differences were observed between the groups of specimens printed at LD and CA filaments. **Second**, the change in nozzle temperature does not have a prominent effect on the flexural strength of the specimens printed with CA filaments; only a slight increase can be observed between the samples printed at 410<sup>0</sup>C and 380<sup>0</sup>C (4.5%). In comparison, an increase in the nozzle temperature resulted in a fair enhancement (18.26 %) in the flexural strengths of the specimens developed from LD filaments, just like the tensile and compressive strength trends. Similarly, the increase in chamber temperature significantly enhanced the flexural strength of the specimen irrespective of the filaments used. **Third**, flexural strengths of the specimens increase with a rise in printing speed, with the highest values observed at 50 mm/sec. The parts printed at the latter speed and LD filaments exhibit a mean flexural strength of 99.25 MPa, almost similar to those printed with CA filaments (101.46 MPa). Fourth, decreasing print layer height thickness enhances the flexural strength of the specimens. In the case of CA filaments, a slight enhancement (3.57%) can be observed over the decrease in the layer height. Instead, in case of LD filaments, a notable difference (16.28%) can be observed between the specimens printed with 0.1 and 0.3-mm layer height. The highest flexural strength was observed in the specimens with 0.1mm layer height with a mean value of 101.23 MPa, almost similar to those printed using CA filaments.

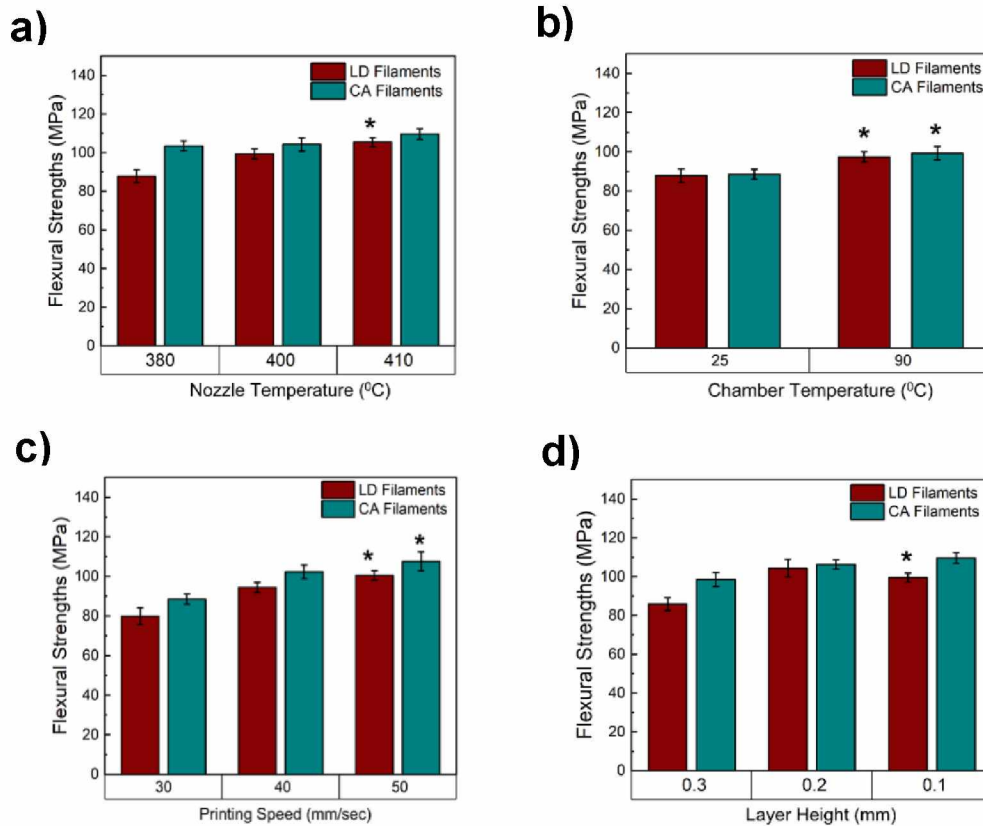


**Figure 1.6:** Comparison of flexural strengths of specimens developed by commercially available (CA) and laboratory developed (LD) filaments as a function of (a) printing speed (b) layer height, and (c) nozzle temperature. \* means that value is statistically significant with the values at 380°C, 25°C, 30 mm/sec, and 0.3 mm

## 1.4 Discussion

In this study, we explored PEEK filaments developed in the laboratory and determined their suitability for 3D printing design-specific structures with favorable mechanical properties. Even though in some cases, the PEEK parts developed with the LD filaments exhibited reduced mechanical properties than the ones developed with CA filaments, overall, the results confirm that favorable quality filaments can be developed in-house, and those can be used in a FDM 3D printer to yield mechanically robust 3D printed parts. One of the primary reasons for the degradation of mechanical properties in the parts printed with LD filaments is the presence of pores or defects in the filament that can be

seen in **Figure 1.7**. The cross-section of a LD filament shows the presence of such defects. Furthermore, the slight inconsistency in the filament diameter also degrades the mechanical properties of the printed parts. For instance, when the filament diameter is thicker than 1.75 mm at a fixed extruder flow, excess material flow results in buildups in the print layers, as seen in the compression specimen (yellow arrows in **Figure 1.8**). That being said, a controlled amount of excess material flow can also promote a robust filament-to-filament bonding in the lateral direction. Yet, an extra flow results in dimensional inaccuracy surface finish and even affects interlayer adhesion. On the other hand, when the feedstock filament was thinner than 1.75 mm, at a fixed extruder flow, it created voids in the print layers due to a shortage in the material flow (red arrows in **Figure 1.8**). These voids are critical in affecting the load distribution between the layers when the specimens are subjected to stress and degrades the mechanical properties.

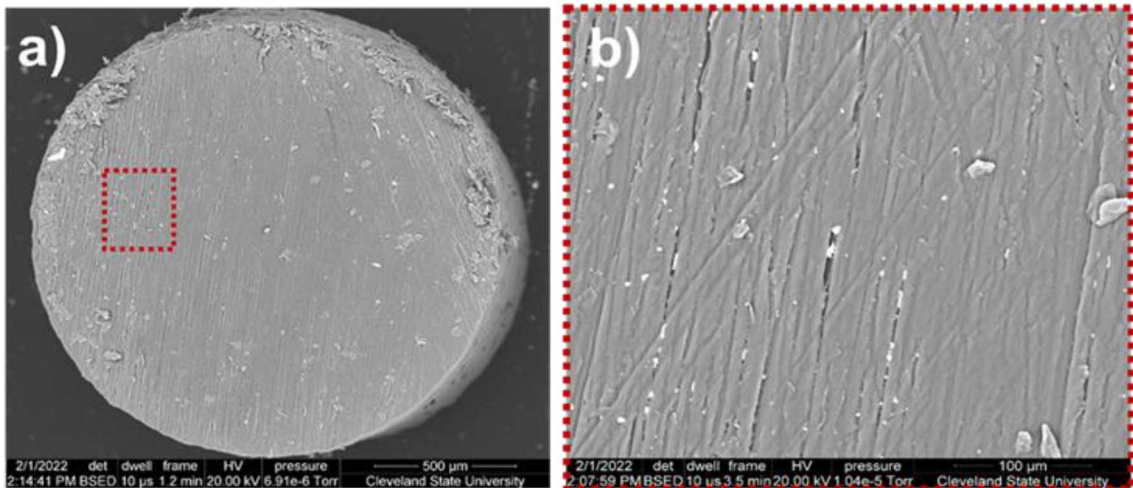


**Figure 1.7:** SEM image showing the cross-section of a LD PEEK filament. A high magnification scan of the red dotted region in (a) is shown in (b). One can notice the pores and defects present in the PEEK filament which causes a detrimental effect on printed structure.

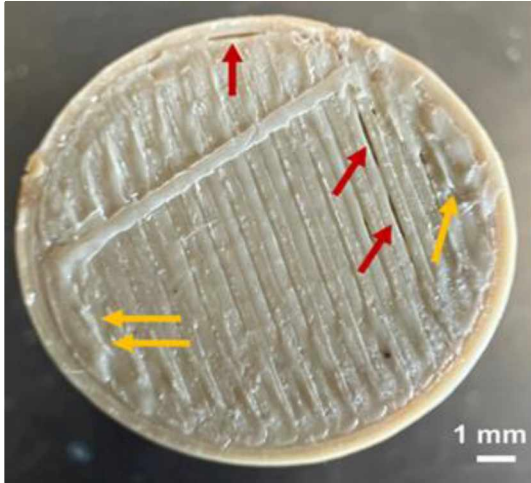


**Figure 1.8:** Photograph of the topmost layer of a 3D printed compression PEEK specimen.

The **Figure 1.8** showing the effect of inconsistencies in filament diameter. Yellow arrows indicate the portions where excess material was deposited due to a thicker filament diameter and red arrows indicate the portions that received lesser material due to thinner filament diameter.

Indeed, it is critical to employ an optimum set of FDM processing parameters to achieve the parts with the best mechanical properties. It is evident that printing parameters such as nozzle temperature, chamber temperature, layer height, and printing speed significantly affect the mechanical properties of the printed structure [20, 26]. Temperatures of the nozzle, build plate, and chamber mainly affects the crystalline/amorphous ratio of the 3D printed PEEK structures [18, 27]. PEEK, similar to many other polymers, is semicrystalline, meaning that PEEK in the solid-state consists of crystalline and amorphous structures, each of which has different characteristics [28]. On the one hand, a completely crystalline structure is characterized by its high molecular order, close polymer chain packing, and strong intermolecular forces. Therefore, the crystalline region in PEEK contributes to having a more dense and rigid polymer. On the other hand,

the amorphous region is characterized by its random and intertwined structure. Thus, the density and mechanical properties of PEEK depend primarily on the crystalline/amorphous ratio [29, 30]. In the present study, all the test specimen parts exhibit a mixture of amorphous and crystalline PEEK, which is indicated by the mix of dark brown and beige-colored regions (**Figure 1.3**). The dark brown indicates the amorphous regions, and the beige region exhibit the crystalline regions. The amorphous and crystalline combination in a single printed part is not appropriate for obtaining excellent mechanical properties. A good way to address this is to anneal the parts post-printing. To analyze the effect of post-heat-treatment, we annealed one set of tensile specimens printed using: Nozzle Temp.: 410<sup>0</sup>C, Chamber Temp:90<sup>0</sup>C, Print Speed: 50 mm/sec, and layer height: 0.1 mm. We observed an enhancement of 7% in the mechanical properties and achieved a tensile strength of 114.34 MPa in the annealed parts. This is because annealing crystallizes the amorphous regions and forms a completely crystallized part corroborated by the uniformly beige colored PEEK specimen shown in **Figure 1.9a**. Further, with the help of our DSC results, we observed a 3.21% rise in crystallinity in the annealed parts as compared to the non-annealed ones. (**Figure 1.9b**). However, we did not anneal the other sets as we wanted to analyze the effect of the printing conditions on the mechanical properties of the specimens.

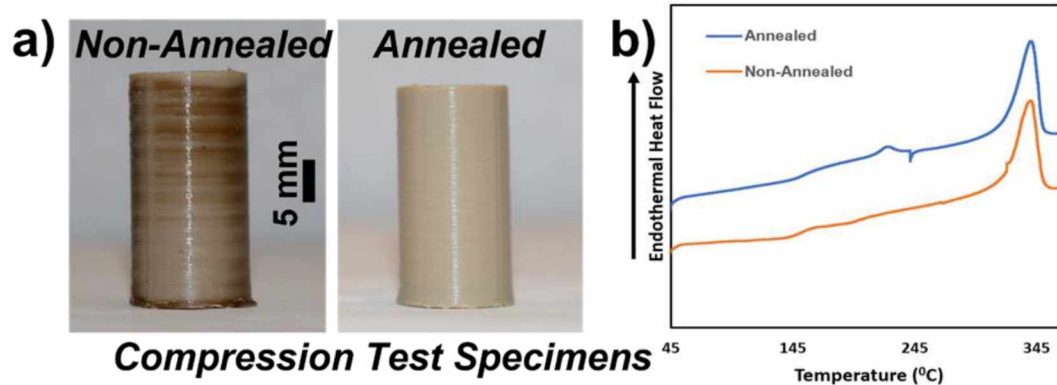


**Figure 1.9:** Effect of annealing on 3D printed PEEK. (a) Photographs of non-annealed and annealed compression test specimen. While the non-annealed part show a mix of amorphous (dark brown color regions) and crystalline regions (beige color regions), the annealed part is totally crystalline (completely beige color). (b) Differential Scanning Calorimetry (DSC) plots of annealed and non-annealed 3D printed PEEK parts. The 3D printing parameters that were used to print this parts are as follows: Nozzle Temp: 4100C, Chamber Temp: 900C, Print Speed: 50 mm/sec, and layer height: 0.2 mm

Along the same lines, the mechanical tests, including compression, tensile, and bending, showed increased mechanical properties by increasing the nozzle temperature, which can also be explained by the higher crystallinity of 3D printed PEEK samples produced by higher printing temperature. Furthermore, higher nozzle temperatures decrease the melt viscosity of the polymer/PEEK extrudate, resulting in easy flow of the material through the nozzle, resulting in better filament deposition and filament-to-filament bonding. Also, a more viscous extrudate helps diffuse well with the underlying polymer layer and promotes a strong filament-to-filament bonding in the lateral and vertical direction [31-33]. Similar results have been shown in a study conducted by Yang et al. focusing on the thermal processing effect on the crystallinity of 3D printed PEEK structure [18]. In that study, 3D printed PEEK tensile bars were printed with nozzle temperatures ranging from 360 °C to 480 °C, and the results showed an increase in PEEK crystallinity from 16% to 21%. Also, the results showed that tensile strength and elastic modulus were



increased when the nozzle temperature increased from 360 °C to 420 °C, accompanied by an increase in crystallinity. However, the tensile properties decreased from nozzle temperature of 440 °C to 480 °C due to material degradation [18]. The degradation of PEEK during the 3D printing process above the nozzle temperature of 430 °C was also captured by Vaezi et al. [17]. A study by Wang et al. [34] investigated the effect of different AM parameters (e.g., nozzle diameter, nozzle temperature, and printing speed) on the mechanical performance of FDM PEEK. Nozzle temperatures of 420 °C, 430 °C, and 440 °C were investigated in the latter study, all of which were more than the highest temperature used in the present study. The authors observed that when optimum printing parameters were combined with the nozzle temperature of 430°C, it produced a structure with higher compression and bending properties compared to the nozzle temperature of 420 °C [34]. In another study, Ding et al. [31] studied the effect of nozzle temperature on the mechanical properties of 3D printed PEEK samples. The nozzle temperature range used in that study was 360 °C to 420 °C with a gradient of 10 °C, similar to the temperature profile explored in the present study. The results showed that the relative density of the printed PEEK samples increased with the increase in nozzle temperature and achieved the highest relative density (92.5%) at the highest nozzle temperature (420 °C). Increasing the nozzle temperature improves the fluidity of the polymer melt through the nozzle and eliminates the air particles, which increase the density of the 3D printed structure and improve the adhesion between the printed layers. In the same study, the results showed that increasing nozzle temperature from 360 °C to 420 °C significantly increased tensile and flexural strengths [31].

Also, in the present study, mechanical properties were enhanced by increasing the chamber temperature. The chamber temperature affects the cooling speed of the printed layers. Thus, it affects the crystallinity of the printed structure. For instance, a 3D printed PEEK structure at a chamber temperature of 25 °C will be cooled faster than a structure printed at 90°C, thus increasing the chamber temperature improves the crystallinity of the 3D printed structure. Hu et al. proposed several design structures to improve the mechanical properties of 3D printed PEEK using finite element analysis [35]. The study showed that PEEK structures printed at a chamber temperature of 60 °C were more crystalline and had better mechanical performance than those printed at 25 °C [35, 36]. Moreover, the strength of interlayer bonding improves when the temperature field is more uniform [35], which can be achieved by increasing the chamber's temperature and printing bed. A study by Wu et al. [13] also investigated the effect of chamber temperature on the 3D printed PEEK structure quality. In that study, the warp deformation of PEEK structures has been monitored versus chamber temperature of 90 °C, 100 °C, 110 °C, 120 °C, and 130 °C. The results showed that increasing the chamber temperature improved the quality of 3D printed structures in which increasing the temperature from 90 °C to 130 °C reduced the warp deformation from 1.93 mm to 0.65 mm [13]. In the present study, 90°C chamber temperature helped in elevating the mechanical properties compared to the 25°C; however, it should be noted that 90°C was not sufficient to yield completely crystalline parts (**Figure 1.3**) with optimum mechanical properties.

The layer height is another important factor that has an inversely proportional relationship with the quality and mechanical performance of the 3D printed structures. Smaller layer height provides a better surface finish of the 3D printed structure [20, 37].

Additionally, smaller layer height produces denser structures that significantly increase the mechanical properties of the printed structures [37]. Liaw et al. studied the effect of different 3D printing parameters on the interlayer bonding strength of the 3D printed PEEK structures [38]. In that study, the 3D printed PEEK structures were printed in the vertical direction then the strength of the interlayer was evaluated by conducting a three-point flexure test where the bending load was applied perpendicular to the printing direction. It was noticed that among all the 3D printing parameters investigated in that study, the layer height was the only parameter that affected the flexure modulus significantly. The results showed that reducing the layer height increased flexure stress at break and flexure modulus. We also observed a similar trend in the present study, where decreasing the layer height increased the compressive, tensile and flexural strengths of the 3D printed PEEK parts. Thinner layers eliminate microvoids between printed layers by reducing the layer height, which results in a closely stacked layer and better bonding [38].

Interestingly, printing speed is a complicated factor that can either improve or hamper the mechanical performance of the printed structure when combined with other specific printing parameters. For instance, higher printing speed with a thick layer height and low nozzle temperature reduces the quality and mechanical properties of the printed structure. However, when a higher printing speed is combined with thinner layer height and high nozzle temperature, it improves the quality and mechanical properties of the printed structure, as this parameter combination decreases the interlayer defects and increases interlayer bonding [19]. Geng et al. studied the effect of the FDM extrusion and printing speeds on the accuracy of the extruded PEEK filament [39]. In that study, defects in 3D printed PEEK straight lines were investigated at different extrusion and printing

speeds. There were evident defects in the printed line at an extrusion speed of 1 mm/min and printing speed of 6.9 mm/min compared to the printed line at an extrusion speed of 80 mm/min and a printing speed of 335.5 mm/min, which has no apparent defects [39]. This is because the melt flow should have a sufficient pressure drop through the liquefier to move out of the nozzle and be deposited on the printing bed. In the case of slow extrusion speed, therefore, slow printing speed, there will be an insufficient pressure drop in the liquefier zone, creating cavities in the filament [39]. Our observations are similar to the previous studies. Higher printing speeds yields better mechanical properties as it helps in reducing the extent of defects in the print layers, ensures a favorable interlayer adhesion and avoids extrudate build-ups. Indeed, the print speed should be optimized as too high speeds might not give sufficient time to deposit the extrudate and even affect the dimensional accuracy resulting in voids.

Thus, in this study, the most favorable printing conditions identified are Nozzle Temp: 410<sup>0</sup>C, Chamber Temp: 90<sup>0</sup>C, Print Speed: 50 mm/sec, and layer height: 0.1 mm. We used this printing combination and LD filaments to print a femoral head, as shown in **Figure 1.10**.

Indeed, we noticed layers with varying amorphous and crystalline regions, but the overall resolution and quality was outstanding, indicating that LD filaments and a combination of optimum 3D printing parameters can yield excellent orthopedic medical devices.



**Figure 1.10:** Photograph of a femoral head as developed by the optimized set of printing parameters (Nozzle temp: 4100C, Chamber temp.: 900C, Printing speed: 50 mm/sec, Layer height: 0.1 mm) and LD filaments.

### **1.5 Conclusion**

In this study, we were successful in making quality PEEK filaments in-house. We did not notice any considerable differences in the mechanical properties of the parts printed with LD and CA filaments in almost all the printing conditions. Yet, the slight decrease in the mechanical properties of the parts printed with LD filaments can be attributed to the defects in the filament and variability in the filament diameter. Notably, an increase in nozzle and chamber temperatures significantly enhances the mechanical properties of the specimens. However, the present study's highest thermal conditions, i.e., 410<sup>0</sup>C nozzle temperature and 90<sup>0</sup>C chamber temperature, were not sufficient to yield completely crystalline PEEK parts. Instead, all the parts contained mix of amorphous and crystalline regions. Also, a high printing speed and lower layer height were promising in considerably improving the mechanical properties of 3D printed PEEK.

## CHAPTER II

### Mechanical Properties of 3D Printed Porous PEEK Orthopedic Scaffolds

#### 2.1 Introduction

Poly-ether-ether-ketone, commonly abbreviated as PEEK, is a member of the poly-aryl-ether-ketone (PAEK) family and was first introduced by Victrix PLC and Imperial Chemical Industries in the early 1980s [40]. It is considered one of the best high-performance polymers primarily due to its outstanding mechanical properties, superior wear resistance, and high resistance to chemical and thermal degradation [1]. PEEK exhibits Young's modulus of around 3.6 GPa, a tensile strength of 90-100 MPa, and a high melting temperature of 343°C [1]. Such properties have promoted PEEK to be the material of choice in many industries such as automobile, aerospace, and chemical.

Over the last few decades, PEEK has also been considered one of the most preferred synthetic materials in the biomedical industry [4]. It is extensively used to make orthopedic and spine implants, such as total joint replacement, fracture fixation devices, and spinal fusion cages. In many instances, PEEK has been proven to be a preferred biomaterial over metals, primarily due to the following reasons. First, PEEK drastically reduces the chances of stress-shielding, a phenomenon highly possible with metallic implants [41]. PEEK has

an elastic modulus of 3.6 GPa, which is near to compact bone (15 GPa) [4], whereas the elastic modulus of titanium (alloys) is 110 GPa which is 5-6 times greater than that of compact bone [42]. As a result, these stiff implants do not adequately strain the bone, resulting in tissue atrophy, bone resorption, and weak bone formation with low density (stress-shielding) [43]. On the contrary, PEEK can be easily tailored to exhibit stiffness close to the bone, thus resolving the problem of stiffness mismatch and consequential stress-shielding [44]. Second, PEEK remains highly stable *in vivo* and does not leach out ions in the bloodstream like metallic implants [45]. Thus, PEEK implants are biocompatible and have less to no chance of causing allergic reactions. Third, PEEK is radiolucent, and hence it lets a straightforward assessment of the bone formation around the implant [46]. However, despite several advantages of PEEK as a biomaterial, its extremely hydrophobic surfaces make it bioinert thus inhibiting PEEK to integrate with neighboring tissue when implanted *in vivo* [23].

Many approaches have been explored to date to make PEEK bioactive. In this regard, surface modifications on PEEK surfaces and PEEK-based composites with bioactive components are the two most researched approaches [47] [48]. Surface modifications such as coating PEEK surfaces with bioactive materials [49-52], sulfonation [53], alkali etching [54], plasma-ion immersion implantation [55], and plasma treatments [56] has exhibited promising results by making PEEK surfaces hydrophilic and bioactive. On the other hand, blending PEEK with bioactive particles such as hydroxyapatite [57] or titanium dioxide [58] to develop composites has been proven effective in developing PEEK-based bioactive implants. However, surface modification strategies have exhibited critical deficiencies such as inflammation and cytotoxicity due to burst release of implanted

ions, exhaustive nature of bioactive agents, and coating delamination [59-61]. In addition, composites face the problem of compromised mechanical properties due to excess secondary material incorporation [62].

On the contrary, bone tissue engineering has extensively utilized porous scaffolds to enhance implant-tissue interaction. The osteogenic capability of the scaffold is greatly enhanced by the interconnected pores, which facilitate cell distribution, nutrient and blood flow, robust anchorage and integration between the neighboring tissue and the implant, and vascularization [63, 64]. However, conventional manufacturing techniques such as salt leaching, gas foaming, phase separation, freeze-drying do not control the pore sizes and number. Also, the formed pores lack interconnectivity which is critical for nutrient flow, cell migration, vascularization, and tissue ingrowth. Notably, scaffolds with random pores and wide variation in pore sizes weaken the scaffold's mechanical strength or load-bearing capacity, thus leading to implant failure.

On the other hand, Additive Manufacturing or 3-dimensional (3D) Printing gives ultimate control to develop scaffolds with precise pore size and number. 3D printing has been utilized to efficiently develop porous PEEK scaffolds with precise pore design and geometry. Specifically, Fused Deposition Modelling (FDM), a type of 3D printing, is a powerful and efficient tool to develop porous scaffolds with enhanced bioactivity. For instance, Su et al. [65] used the FDM-based 3D printing technique to develop a porous PEEK scaffold which helped in enhanced bone formation *in vivo*. However, the authors primarily credited the microporous architecture of the 3D printed scaffolds caused by sulfonation to facilitate osseointegration. Spece et al. [66] used the FDM technique to develop porous PEEK with pore designs based on a simple rectilinear pattern, gyroid, and



diamond types (triple periodic minimal surfaces) to mimic the morphology of trabecular bone in pore size and porosity and reported enhanced pre-osteoblast activity on the porous scaffolds as opposed to the solid ones. In a critical study, Fen et al. [67] developed porous PEEK scaffolds by the FDM method with different pore sizes (300, 450, and 600 $\mu\text{m}$ ). Using a rabbit model with distal femoral condyle defects, the authors prove that PEEK scaffolds with 450  $\mu\text{m}$  pore sizes were apt for bone ingrowth and vascular perfusion [67]. Recently, Liu et al. [68] also used the FDM to create porous PEEK scaffolds (700  $\mu\text{m}$  pore size) and then used sulfonation and UV-induced graft polymerization to develop methacrylated chitosan/polyhedral oligomeric silsesquioxane nanocomposites. With the help of the rat calvaria defect repair model, the authors confirmed that the 3D printed, treated PEEK scaffolds promoted osteogenesis [68]. Elhatab et al. [5] also used FDM to develop PEEK scaffolds with various pore sizes and reported that 800  $\mu\text{m}$  pore size is optimal for pre-osteoblast adhesion and proliferation [5].

However, it is well-known that porous scaffolds will exhibit lower mechanical properties than their non-porous solid counterparts, which can be detrimental to the load-bearing capacity of the scaffolds. In addition, pore sizes play a significant role in influencing the biological and mechanical properties of the scaffolds. For instance, smaller pores may inhibit cell proliferation or lead to insufficient vascularization and nutrient transport *in vivo*, whereas larger pores may decrease scaffold load-bearing capacity and significantly affect fatigue lifetime [69, 70]. Therefore, it is essential to develop porous scaffolds with optimum pore sizes to help in osseointegration without compromising the desired mechanical properties. Yet, only a few studies have explored the mechanical properties of PEEK porous scaffolds developed by FDM [17, 66]. Moreover, very few

studies have analyzed the effect of pore sizes on the FDM-developed PEEK scaffolds' mechanical properties [67]. Hence, in this study, we used the FDM technique to develop PEEK scaffolds with a wide variety of pore sizes starting from 100 to 600  $\mu\text{m}$ . Subsequently, we experimentally determined the compressive strength of the scaffolds. We then used the Finite Element Analysis (FEA) to model the compressive properties of the scaffolds and establish the influence of pore sizes on the compressive properties of the FDM-developed PEEK scaffolds.

## **2.2 Materials and Methods**

### **2.2.1 Raw Materials for 3D Printing**

A commercially available PEEK filament with a diameter of 1.75 mm (Thermax<sup>TM</sup> PEEK Natural, 3DXTECH) was used for 3D printing of all the samples. The filaments were dried at 120<sup>0</sup>C for 5h before using them for 3D printing.

### **2.2.2 FDM-3D Printing Parameters**

We used a FUNMAT HT Enhanced (Intamsys Technology Ltd., Shanghai, China) for 3D printing various PEEK specimens for mechanical testing. The following FDM parameters were followed for 3D printing the scaffolds. Annealing was not performed on the printed specimens.

**Table 2.1:** FDM Parameters used for printing the PEEK Scaffolds.

<i>Parameters</i>	<i>Values</i>
Nozzle Temperature	400°C
Chamber Temperature	90°C
Bed Plate Temperature	130°C
Layer Height	0.2 mm
Printing Speed	50 mm/sec

Cylindrical PEEK scaffolds with four different pore sizes were explored: 100, 300, 500, 600  $\mu\text{m}$  were developed. A  $\text{\O} 0.2$  mm nozzle was used to print the scaffolds with pore sizes of 100  $\mu\text{m}$  and a  $\text{\O} 0.4$  mm nozzle was used to print the scaffolds with 300, 500, and 600  $\mu\text{m}$  pore sizes. The specific pore sizes were printed by varying the distance between the infill strands using the slicing software (Simplify 3D). The dimensions of the infill strands were also controlled accordingly depending on the pore sizes of the scaffolds. The cylindrical scaffolds used for physical characterization were  $\text{\O}15$  mm and 10 mm in height. The scaffolds which underwent compression testing were  $\text{\O}12.3$  mm and 24.6 mm in height as per ASTM D695 [24]. The Instron 3369 Universal Testing Machine (UTM) was used for the uniaxial compression testing, and a constant displacement of 1.27 mm/min was used for the tests. Stress-strain curves were generated from the data collected, and the elastic region was used for determining Young's modulus of the specimens. The porous specimens' yield compressive strength was also determined (taken as the 0.2% offset stress) [71].

### 2.2.3 Physical Characterization

The 3D printed scaffolds were first inspected by a stereomicroscope (SM-1TSZZ-144S-10M, AmScope, Irvine, California) and then using a field-emission scanning electron microscope (FESEM, Inspect F50, FEI, Oregon, United States). Pore sizes were measured using the FESEM's inbuilt software.

### 2.2.4 Finite Element Analysis

The 3D models of the cylindrical PEEK scaffolds with varying pore sizes were developed in Solid Works and then imported into Abaqus Finite Element (Abaqus, 2013) for numerical analysis. The inbuilt homogeneous, isotropic, elasto-plastic material model was used to represent the non-linear behavior of PEEK [72]. Model parameters are stated in **Table 2.2**; these values were based on the prior experimental uniaxial stress-strain response of a dog bone specimen tested under tensile loading and compression testing of sample scaffolds. Since the present study focused on the influence of the macro-pores on the structural responses of the PEEK scaffolds, other effects from temperature differences, loading rate, etc., were not presently considered. After testing several different three-dimensional element types and conducting a convergence study, the general purpose linear brick fully integrated continuum element (C3D8) constituted the major part of the element type. A minimum average mesh size of 300  $\mu\text{m}$  was maintained in all simulated cases; hence, the number of elements varied based on the scaffold pore size. The appropriate boundary conditions were applied to allow compression in the longitudinal Z-direction. In this process, one face of the scaffold was fixed against translation and rotation, while the other face was subjected to uniform displacement ( $\delta$ ) at a rate of 1.27mm/min.

**Table 2.2:** Abaqus isotropic, elasto-plastic model parameters.

<i>Property</i>	<i>Value</i>
Elastic Modulus, E	502-3000 MPa
Poisson's ratio	0.35
Yield stress	20-90 MPa

A quasi-static non-linear analysis was conducted using a maximum time increment size of 0.5. The displacements were increased until the analysis ended, and the maximum reaction forces were evaluated. To capture the behavior of material within the elastic region, the forces at selected displacements within the linear elastic range were also recorded for each scaffold case. Moreover, the buckling linear perturbation analysis with subspace eigensolver was used to obtain the first three buckling loads and modes.

### **2.2.5 Statistical Analysis**

Statistical differences between the properties of 3D printed specimens with different pore sizes were determined using Student's t-test and one-way ANOVA. Significance was determined at  $p > 0.05$ .

## **2.3 Results and Discussion**

### **2.3.1 Porous Scaffold Morphology**

**Figure 2.1(a-d)** shows the stereomicroscope and SEM images of the porous PEEK scaffolds. The stereomicroscope images confirm the development of uniform porous PEEK scaffolds with no pore-clogging. Notably, the scaffold with the smallest pore size, i.e., 100  $\mu\text{m}$  pore size, did not experience pore-clogging to the slightest extent. Furthermore, all the scaffolds exhibited a uniform distribution of the infill strands resulting in a consistent

rectilinear pattern. The SEM images give a more magnified view of the pore geometry and size distribution. The pore geometry was primarily square, and qualitatively, the pore sizes appeared to be uniform. **Table 2.3** shows the pore size distribution of the designed and the actual scaffolds as calculated by the FESEM software. For every scaffold, the average pore size showed no significant difference ( $p > 0.05$ ) as compared to the as-designed size, indicating the high precision of the FDM-3D printer. Moreover, 100% interconnectivity for all the porous specimens was indicated through the passage of natural light. Overall, FDM-3D printing was capable of printing porous PEEK scaffolds with uniform pore size and geometry.

### **2.3.2 Mechanical Properties**

The primary failure mode for the porous PEEK scaffolds was successive layer collapse caused by buckling of the cylindrical specimens. The stress-strain curves of the porous specimens are shown in **Figure 2.2**. The porous specimens exhibited the typical behavior of porous materials, with a linear elastic region followed by a plateau and then a sharp increase in stress mainly as the specimens become compressed and densified. We did not observe any major fluctuations in stress in the plateau or the elevated stress region. However, minor fluctuations were observed in the specimens with 300, 500, and 600  $\mu\text{m}$  pore sizes. The stress fluctuations in the plateau region result from the collapse of the struts one at a time under the load. These observations are consistent with the recent study by Spece et al.[66].

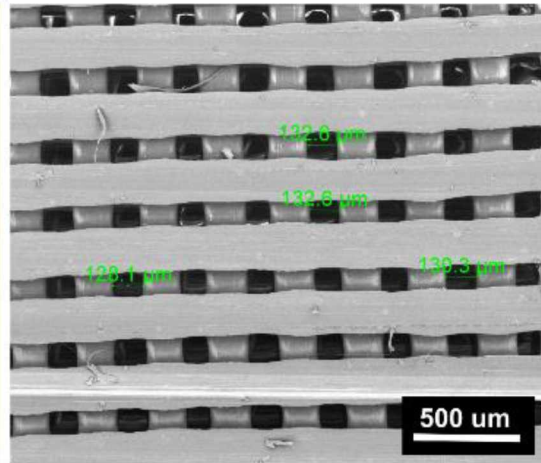
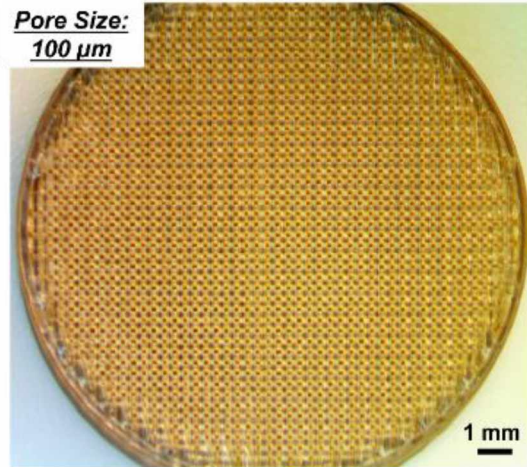


Figure 2.1a

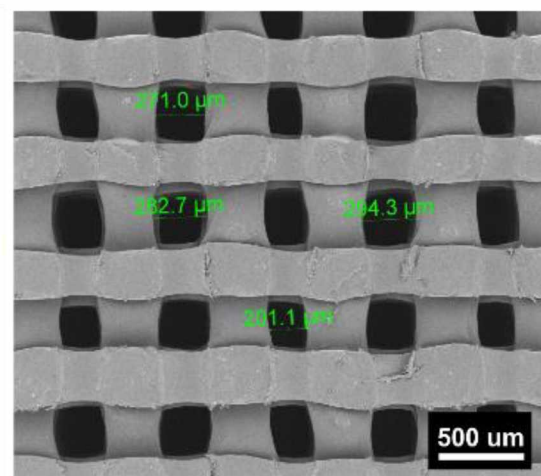
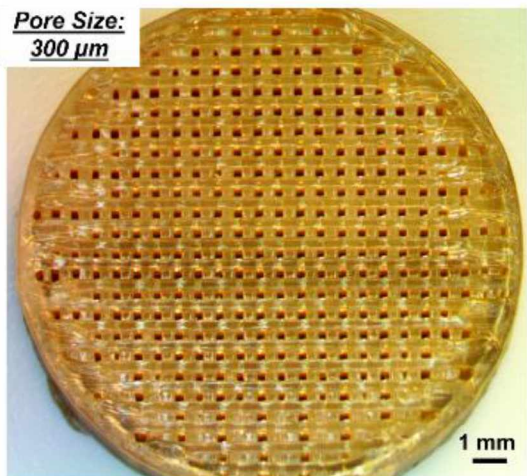


Figure 2.1b

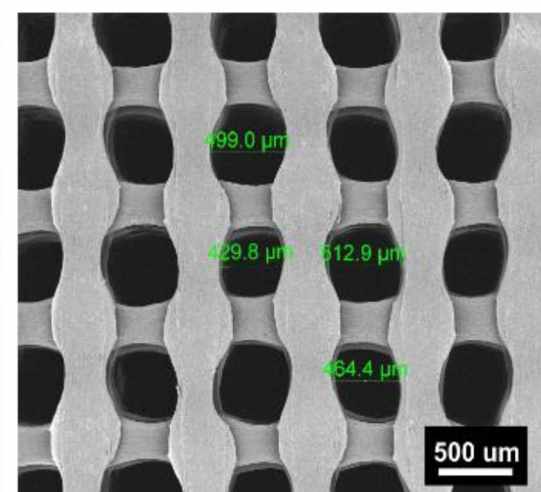
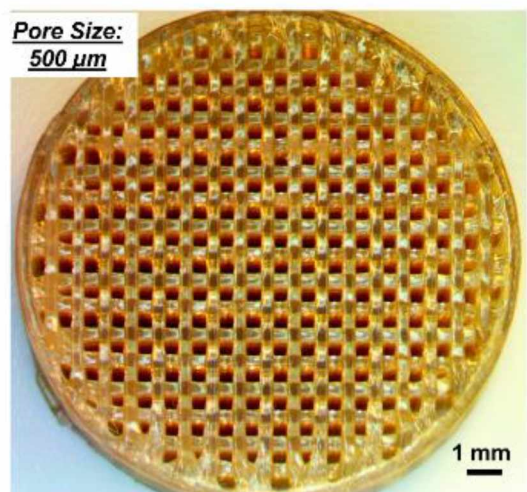
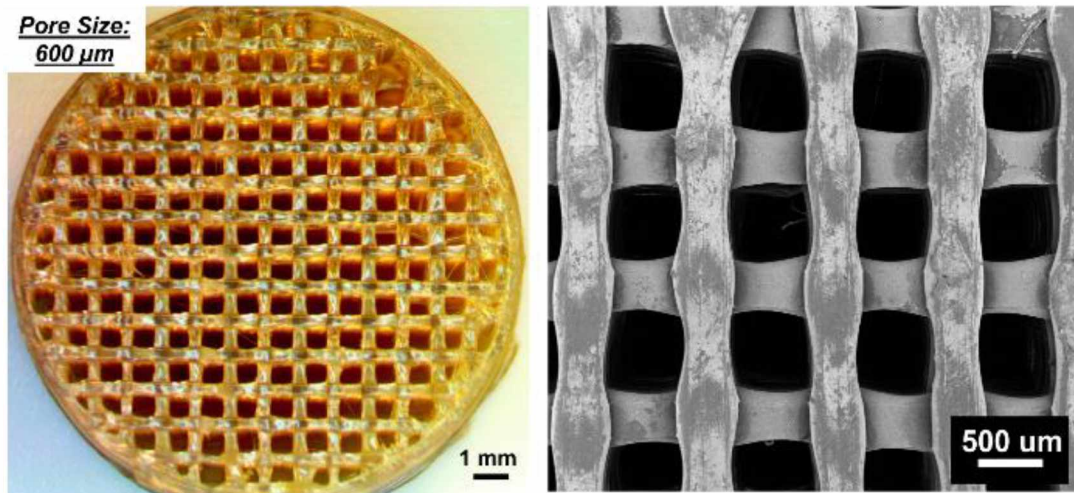


Figure 2.1c



**Figure 2.1d**

**Figure 2.1:** Stereomicroscopy and corresponding Scanning Electron Microscopy (SEM) images of the 3D printed PEEK porous scaffold.

**Table 2.3:** Pore Size Distribution of the 3D printed porous scaffolds.

<i>Designed</i>	<i>Actual</i>
100 $\mu\text{m}$	$128.15 \pm 5.67 \mu\text{m}$
300 $\mu\text{m}$	$282.45 \pm 16.74 \mu\text{m}$
500 $\mu\text{m}$	$495.25 \pm 30.54 \mu\text{m}$
600 $\mu\text{m}$	$614.35 \pm 41.23 \mu\text{m}$



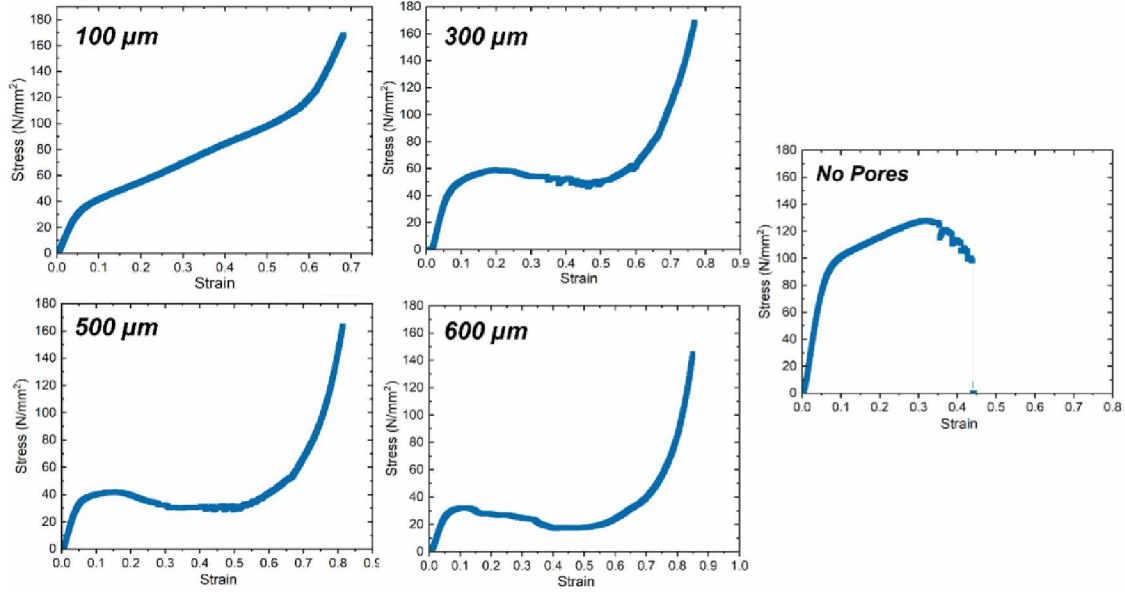


**Figure 2.2:** Stress-Strain Curves of porous PEEK specimens with different pore sizes under compression loading. Specimen with no pores is shown for comparison.

**Figure 2.3** shows the average yield compressive strengths of the specimens. An interesting trend can be noted. The specimens with 100  $\mu\text{m}$  pore size exhibited an average yield strength of 32.67 MPa; while the specimens with 300  $\mu\text{m}$  pore size showed the highest average yield strength of 41.59 MPa in the cohort of porous specimens. However, the compressive strengths decrease hereafter as the pore size increases. Average yield strength of 35.47 MPa and 28.69 MPa was observed for the specimens with 500 and 600  $\mu\text{m}$  pore sizes, respectively. In the case of the Young's modulus, the trend was similar. Specimens with 100  $\mu\text{m}$  pore size exhibited an average Young's modulus of 628 MPa. The highest average Young's modulus of 791.85 MPa was observed in the case of the porous specimens with 300  $\mu\text{m}$  pore sizes. Specimens with 500 and 600  $\mu\text{m}$  pore sizes recorded an average Young's modulus of 645.27 MPa and 570.03 MPa, respectively. Notably, the specimen with 300  $\mu\text{m}$  pore size exhibited significantly greater strengths and Young's modulus than the specimens with 600  $\mu\text{m}$  pore size. For comparison purposes, the solid

PEEK specimens' mechanical properties are also included in **Figures 2.2** and **2.3**. The stress-strain curve of the non-porous PEEK scaffolds (i.e., does not have any designed pores) displays the typical stress-strain nature of rigid and robust thermoplastics. A linear elastic region is observed, followed by the elevated plateau, i.e., the strain hardening region and the necking region. The average yield compressive strength and Young's modulus of the non-porous PEEK scaffold were recorded as 90.59 MPa and 3003.78 MPa, respectively. As expected, the non-porous specimens exhibited significantly higher yield strengths and Young's modulus values than all the porous specimens.

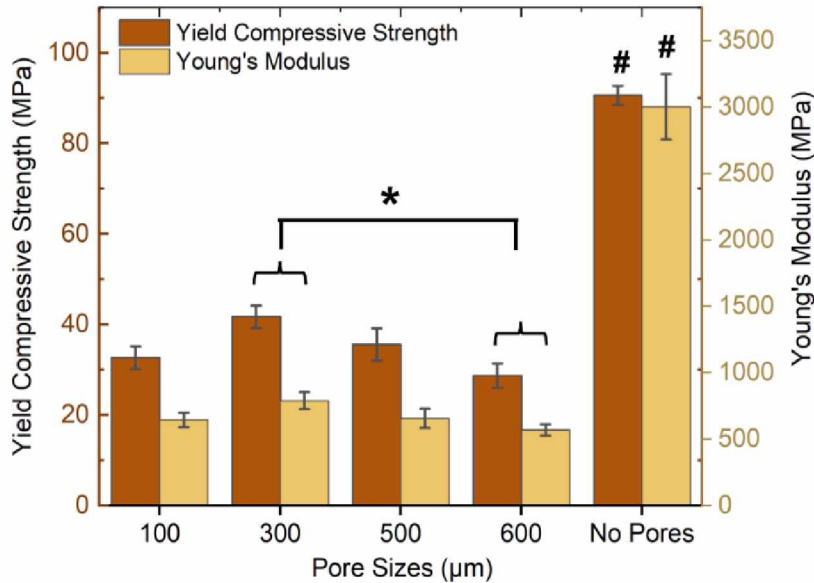


**Figure 2.3:** Yield compressive strength and Young's Modulus of porous PEEK specimens with different pore sizes. \* Indicates statistically significant with respect to the specimens in that group. # indicates statistically significant with respect to all the porous specimens.

The results of the present study are consistent with previously published reports. For instance, Feng et al. [67] developed PEEK scaffolds with 300, 450, and 600 μm pore sizes and observed the compressive Young's modulus and compressive strength of the samples decreased with the increase in the pore size. The yield strength values of the porous specimens were also comparable with the ones in the present study. However, the

compressive strength for PEEK scaffolds with 300  $\mu\text{m}$  pores was reported to be 59.9 MPa, which is notably higher when compared to the compression strength values of the present study. However, the scaffolds with 600  $\mu\text{m}$  pore sizes were comparable to the ones in the present study. Interestingly, the elastic modulus for the porous PEEK scaffolds (367.8-231.1 MPa) was lower than the elastic modulus values of the specimens developed in the present study. In another study, Liu et al. [68] developed porous PEEK scaffolds with 700  $\mu\text{m}$  pore size and reported a compressive strength of 15.41 MPa. In the present study, we didn't develop scaffolds with pore sizes above 600  $\mu\text{m}$  as we observed a significant decrease in compressive strengths. Thus, it is recommended not to increase the pore size above 600  $\mu\text{m}$ . Nevertheless, in addition to the pore size, the design of the porous scaffolds also plays a significant role in influencing the compressive strengths of the scaffolds. Spece et al. [66] developed porous PEEK structures of different designs and a fixed 600  $\mu\text{m}$  pore size. The authors observed the lowest mechanical properties in the case of the rectilinear designed scaffolds. Such scaffolds can be compared to some extent with the design of the porous scaffolds in the present study. Notably, the scaffolds with the rectilinear pattern in their study exhibited a yield strength of 6.6 MPa, which is remarkably lower than the yield strength of the 600  $\mu\text{m}$  pore-sized scaffolds developed in the present study (28.69 MPa). This might be because the scaffolds developed in the present case comprised an outer (perimeter) shell, which helped enhance the scaffold's load-bearing capability.

It should also be noted that the scaffold's mechanical properties are also attributed to the selection of the FDM-3D printing parameters such as the thermal processing parameters like nozzle, bedplate, and chamber temperature [18]. In the present case, the 3D printing parameters selected in the present study yielded porous PEEK constructs with

favorable mechanical properties, which might be a reason to achieve scaffolds with better mechanical properties than other studies.

According to the trend that larger pore size decreases the mechanical properties, we should have noticed the highest compressive strength for the 100  $\mu\text{m}$ -sized scaffolds, but we did not. A possible explanation could be that the 100  $\mu\text{m}$ -sized scaffolds comprised a higher number of pores than the 300  $\mu\text{m}$ -sized scaffolds, which decreased the load-bearing capacity of the scaffolds. Also, more infill strands in the 100  $\mu\text{m}$ -sized scaffolds could lead to higher 3D printing defects such as geometrical inaccuracies and insufficient layer adhesion. Yet, overall, the compressive strength values obtained in the present study are relevant to the structural application of the scaffolds. The results indicate a critical consideration in PEEK implant design, i.e. larger pores produce more and larger fatigue cracks than small pores and, therefore, might negatively affect the fatigue lifespan [70] [67, 73]. These results indicated that the pore sizes significantly affect the specimens' compressive stress and elastic modulus. Combinedly, the mechanical properties of the porous PEEK scaffolds verified that PEEK scaffolds with 300 and 500  $\mu\text{m}$  pore sizes have the potential to bear greater physiological loads with less risk of failure than PEEK scaffolds with 100 and 600  $\mu\text{m}$  pore sizes. However, there are some limitations in our analyses; for instance, all mechanical tests were performed in air at room temperature rather than in a more physiological environment. Indeed, the strengths of the scaffolds were lesser than the strength of cortical bone (90-200 MPa) and more than the strengths of cancellous bone (1.5-45 MPa) [74]. The 3D printed porous PEEK scaffolds with 300 and 500  $\mu\text{m}$  pore sizes will be able to withstand partial strength and decrease chances of stress shielding under physiological loading

### 2.3.3 Finite Element Analysis

The 3D rendered images of the porous scaffolds as developed by Solidworks is shown in **Figure 2.4a**. The 3D designs were then imported into Abaqus Finite Element (Abaqus, 2013, V6.13. Analysis user's manual. Providence, RI, USA: Abaqus Inc.; 2013.) for numerical analysis. **Figure 2.4b** shows the example of a cross-section and extruded view of a typical porous scaffold geometry imported into Abaqus. **Figure 2.4c** shows the 2D/cross-sectional view of the porous scaffolds. The behavior of the PEEK specimens was described by classical von Mises plasticity theory. We performed two different sets of analysis; one group had a fixed Young's modulus of 3000 MPa as determined experimentally, and another set had variable Young's modulus of the porous specimens. In these two sets of simulations, the Poisson ratio was set to 0.3, a typical PEEK value [4].

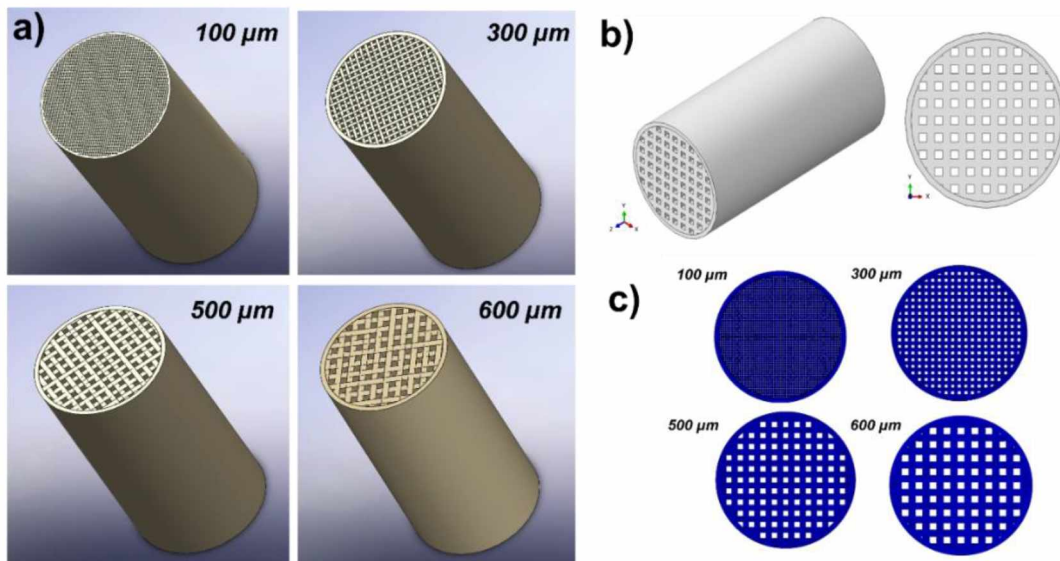


**Figure 2.4:** (a) 3D rendered images of the scaffolds as designed in Solidworks. (b) Typical scaffold geometry used for the finite element study in Abaqus. The images show the extruded view and cross-sectional view of the porous scaffold. (c) Sectional view of scaffold with different pore sizes used for the Finite Element Analyses.

### 2.3.3.1 Yield Compressive Strength

**Table 2.4** shows the yield compression strength values of the porous specimens with constant modulus. It is evident that the FEA significantly overestimated the yield strength values of the porous PEEK specimens when constant Young's modulus is considered. However, the FEA results of the yield strengths are much closer to the experimental ones when Young's modulus is varied depending on the pore sizes, as shown in **Table 2.5**. The results indicate two critical observations. First, inherent Young's modulus of the material should not be used in FEA models when considering porous specimens with different pore sizes as PEEK's inherent Young's modulus (approx. 3GPa) is relatively higher than the porous scaffolds, and this resulted in much higher yield strength value prediction by FEA than the experimental ones. Our results confirm that Young's modulus values are distinct to the structures with different pore sizes and hence should be first determined by real-time experiments and then used in FEA calculations. Second, our FEA models considered extruded continuous structures, whereas 3D printed structures are layered in nature. The porous PEEK scaffolds were developed by a layer-by-layer additive approach (FDM), and this technique of fabrication is evident to develop products with lower mechanical properties than continuous parts like injection molded parts (as considered in the present FEA calculations) [12, 16]. Basically, as layers are glued on to each other to develop the final structure, the mechanical properties of 3D printed parts are strongly influenced by the layer adhesion strength [39]. In the present case of FEA, we worked with a continuous solid structure that is evident to predict higher yield strengths than the experimental values of the 3D printed PEEK structures. Furthermore, it should also be noted that 3D printing parameters can affect the microstructure and lead to defects,

thus reducing the mechanical properties [19]. However, such 3D printing defects are not considered in the FEA model. Gonzalez and Nuno [75] observed significant overestimation of elastic moduli in porous materials with their FEA models and attributed the discrepancy to the irregularities caused by 3D printing, which are not usually accounted for in the FE model. The authors recommended considering manufacturing irregularities in the FEA models to closely predict the mechanical behavior of porous structures. Campoli et al. [76] observed an overestimation of the mechanical properties and demonstrated that structural irregularities could strongly influence the mechanical response of porous materials. In the present case, 3D printing defects are believed to be the factor for reduced mechanical properties in the experimental results. However, using experimental Young's modulus values in the FEA models provided yield strength values close to the experimental values (Table 2.5).

**Table 2.4:** Compression strength of the porous PEEK specimens from FEA simulations with constant Young's Modulus=3000 MPa.

<i>Pore size (<math>\mu\text{m}</math>)</i>	<i>Elastic Regime (MPa)</i>	<i>Inelastic Regime (MPa)</i>
<b>600</b>	68.7	74.2
<b>500</b>	69.7	75.7
<b>300</b>	69.5	73.5
<b>100</b>	70.8	76.8

**Table 2.5:** Compression strength of the porous PEEK specimens from FEA simulations with variable Young's Modulus.

<b>Pore size (<math>\mu\text{m}</math>)</b>	<b><i>Young's modulus (MPa)</i></b>	<b><i>Elastic regime (MPa)</i></b>	<b><i>Inelastic Regime (MPa)</i></b>
<b>600</b>	502	24.704	29.770
<b>500</b>	688	32.83	39.77
<b>300</b>	665	32.87	51.46
<b>100</b>	629	23.655	33.9

### 2.3.3.2 Stress Distribution Analysis

FEA provided us with important stress distribution results. **Figure 2.5(a-c)** shows the stress distribution of the porous scaffolds with different pore sizes in the elastic and non-elastic regions of deformation. The cross-section images of the scaffolds further show the stress distribution within the scaffold core. Some critical observations can be made from the simulations. First, the stresses were higher within the scaffold core than the outer circumference (except the edges close to the fixed support and the part where the displacement was applied). Specifically, the highest stresses occurred longitudinally along the infill strands. This is a strong indication that under compressive load, the initial failure originates within the scaffold rather than the outer shell of the scaffold. As the compressive forces were increased and the scaffolds transitioned into the inelastic (plastic) zone, higher stress distribution was observed within the scaffolds. Notably, in the inelastic region, the von Mises stresses were found to be well above the initial yield strength of the material. Second, when compared with the scaffolds with different pore sizes, the FEA simulations indicated that the von Mises stress distribution was least in the scaffolds with 300  $\mu\text{m}$  pore



sizes, both in the elastic and inelastic region. This denotes that the 300  $\mu\text{m}$  pore-sized scaffolds can bear the maximum compressive forces with a yield strength of 32.87 MPa in the elastic region and 51.46 MPa in the inelastic region, as determined by FEA (**Table 2.5**). This result is on par with the experimental values as the scaffolds with 300  $\mu\text{m}$  pore-sized scaffolds exhibited the highest experimental yield strength of 41.59 MPa. Notably, the stress distribution analysis of this scaffold in the inelastic region also shows a slight deformation, indicating that the scaffold can undergo much higher compressive loads in the inelastic region, as confirmed by its yield strength value of 51.46 MPa (**Table 2.5**). On the contrary, the scaffolds with the highest pore size (i.e., 600  $\mu\text{m}$ ) exhibit the lowest yield strength of 24.704 MPa in the elastic portion of deformation. The latter result is corroborated by the stress distribution analysis in **Figure 2.5c**. The von Mises stress distribution analysis of the scaffolds with 600  $\mu\text{m}$  pore sizes shows that the stress distribution extent within the scaffold core and the outer shell was the highest compared to all the other porous scaffolds. Third, the behavior of the scaffolds in the elastic and inelastic regions was not significantly different, except for the scaffolds with 300  $\mu\text{m}$  pore size. Except for the latter case, the porous scaffolds exhibited similar yield strengths in the elastic and inelastic regions.

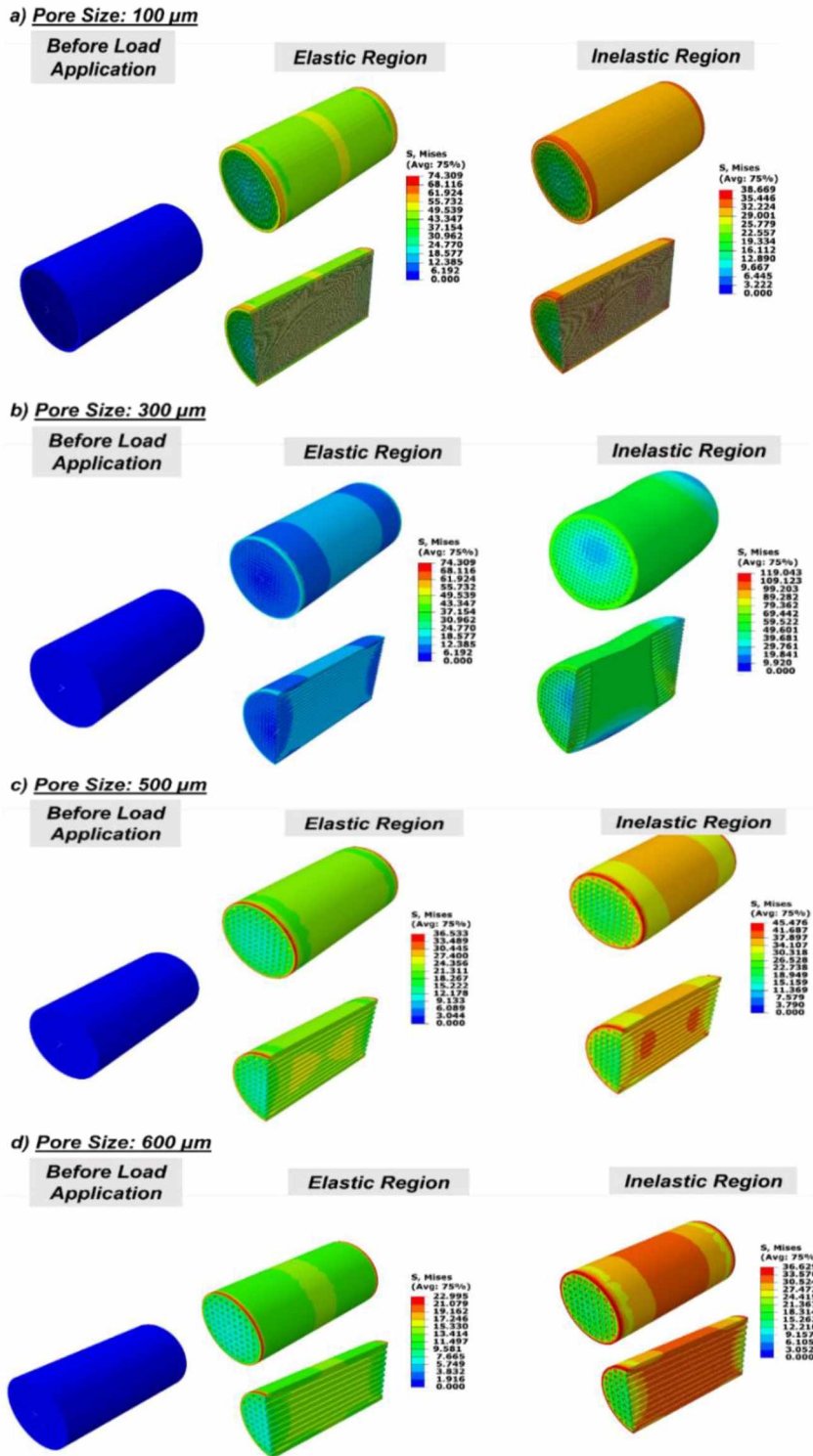


**Figure 2.5:** Finite Element Analysis results of the PEEK porous specimens. von Mises stress distribution results in the 3D printed porous PEEK specimens with different pore sizes such as **a)** 100  $\mu\text{m}$ , **b)** 300  $\mu\text{m}$ , **c)** 500  $\mu\text{m}$ , and **d)** 600  $\mu\text{m}$ .

Previous studies have reported that effective plastic strain develops within the porous network of stochastic foam scaffolds developed by conventional manufacturing techniques [77, 78]. In such scaffolds, plastic strain results near the boundaries of the random pores that result in collapsing the scaffold. The authors of those studies attributed the failure to the non-uniform stress distribution in the random pores generated by conventional manufacturing methods. On the contrary, we did not observe non-uniform stress distributions in the scaffold core. This is because 3D printing helps form porous scaffolds with uniform pore size and shape. The uniform pores in the 3D printed structure provide a homogeneous response in terms of stress, minimizing the probability of early failure and providing a better strength to weight ratio [79].

#### **2.3.3.3 Buckling Nature**

We analyzed the buckling nature of the porous PEEK specimens at three modes. **Figure 2.6b** shows the specimen deformation pattern at the three modes. The specimen bends along the longitudinal axis in the 1<sup>st</sup> mode. In the 2<sup>nd</sup> mode and 3<sup>rd</sup> mode, two and three curvatures can be identified, respectively. The real-time experimental results of the specimens at the end of the compression tests are shown in **Figure 2.6a**. The digital images confirm that under compressive loads, the specimens failed by buckling with two curvatures as per the FEA results in the 2<sup>nd</sup> mode. Notably, at certain locations in the printed structure, layer delamination can be observed, which is an important reason for the failure of the 3D printed specimens. The simulation results did not observe such failure points as a layered structure was not considered for the FE calculations.

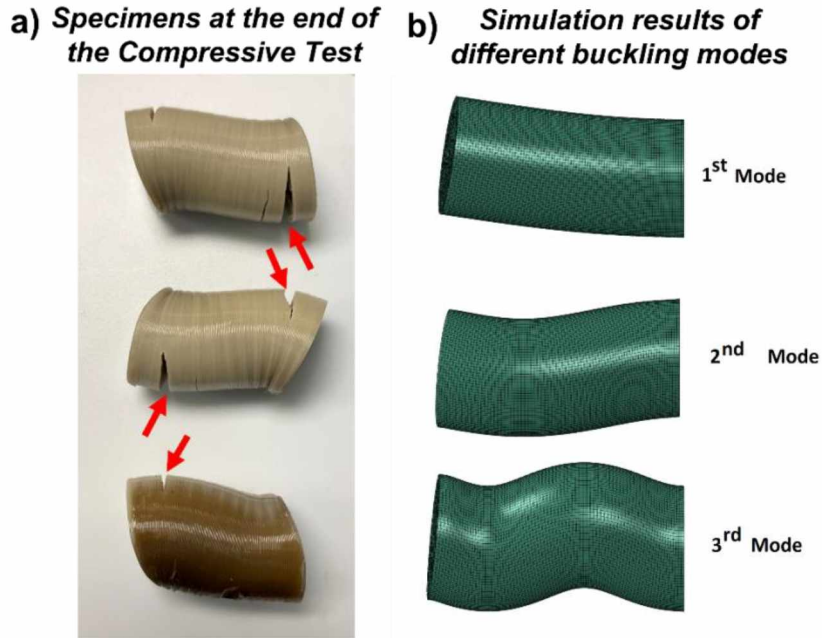


**Figure 2.6:** Failure modes of the 3D printed PEEK specimens. a) Digital photographs of the compression testing specimens at the end of the uniaxial compression testing experiments. The specimens fail by buckling. The red arrows indicate layer debonding as the failure mode in the specimens. b) Simulation results as obtained from FEA show the different buckling modes of the porous PEEK specimens. Of note, the specimens in real-time fail according to the 2<sup>nd</sup> buckling mode as indicated by the simulations.

**Tables 2.6 and 2.7** show the load at which the specimens buckle at the different modes, when constant and variable Young's modulus is considered. When constant Young's modulus is considered, during the 1<sup>st</sup> mode, scaffolds with 600 and 500  $\mu\text{m}$  pore sizes exhibit a much higher buckling load of 2410 N and 2408.3 N than the scaffolds with 300  $\mu\text{m}$  pore sizes. However, in the second mode, which is the primary mode of the specimens' failure, the scaffolds with 300 and 100  $\mu\text{m}$  pore sizes reveal notably higher buckling load than the scaffolds with 500 and 600  $\mu\text{m}$  pore sizes. **Table 2.7** shows the buckling load values of the various scaffolds with specimen-specific Young's modulus. During the 1<sup>st</sup> mode, scaffolds with 300  $\mu\text{m}$  pore size exhibit a value of 2320 N which is close to the highest buckling load experienced by the scaffolds with 500  $\mu\text{m}$  pore size

(2408.3 MPa). However, in the 2<sup>nd</sup> mode, the scaffolds with 300  $\mu\text{m}$  pore size exhibit the highest buckling load of 12870 MPa among all the porous specimens. The results indicate two critical observations. First, the scaffolds with 300  $\mu\text{m}$  pore size can withstand the highest compressive load. Second, porous PEEK specimens fail by the 2<sup>nd</sup> mode of buckling.

**Table 2.6:** Buckling Loads of the porous PEEK specimens from FEA simulations with constant Young's Modulus=688 MPa.

<i>Pore size (<math>\mu\text{m}</math>)</i>	<i>Buckling Load (N) 1<sup>st</sup> Mode</i>	<i>Buckling Load (N) 2<sup>nd</sup> Mode</i>	<i>Buckling Load (N) 3<sup>rd</sup> Mode</i>
<b>600</b>	2410	12806	19877
<b>500</b>	2408.3	12776	19811
<b>300</b>	2398.3	13307	-
<b>100</b>	2405.1	13451	21743

**Table 2.7:** Buckling Loads of the porous PEEK specimens from FEA simulations with variable Young's Modulus.

<b>Pore size (<math>\mu\text{m}</math>)</b>	<b>Young's modulus (MPa)</b>	<i>Buckling Load (N) 1<sup>st</sup> Mode</i>	<i>Buckling Load (N) 2<sup>nd</sup> Mode</i>	<i>Buckling Load (N) 3<sup>rd</sup> Mode</i>
<b>600</b>	502	1760	9352	14520
<b>500</b>	688	2408.3	12776	19811
<b>300</b>	665	2320	12870	-
<b>100</b>	629	2199.4	12301	19844

The FEA simulation results and the experimental results confirm that the porous PEEK specimens fail by buckling, according to previously published results [66]. Four

fracture modes are typically observed in 3D printed PEEK and PEEK-based composites: (1) ductile fractures; (2) layer debonding induced by shear deformation and dissatisfactory interlayer adhesion; (3) layer debonding caused by buckling; and (4) semi-brittle fractures [80]. In the present study, layer debonding induced by buckling was observed to be the prominent failure mode. As mentioned before, we did not consider a layered structure hence layer debonding was not recorded in the simulation results. It is recommended that for 3D printed structures, FEA modeling should consider a layered structure and even include common 3D printing irregularities such as filament voids or interlayer porosity. Consideration of these factors in the FEA models will help in predicting the failure modes of the scaffolds more realistically.

When developing load-bearing orthopedic implants, it becomes critical to design high-strength scaffolds that can bear continuous physiological loads. At the same time, it needs to be engineered so that it does not exhibit stress-shielding, promotes bone regeneration around the implant area, and supports robust osseointegration. In this study, we 3D printed porous PEEK scaffolds that can effectively help in osseointegration without compromising their mechanical properties. The experimental and FEA results indicate that the scaffold with 300  $\mu\text{m}$  pore size exhibits the highest mechanical property in the cohort of porous specimens explored in this study. Increasing the pore size above 300  $\mu\text{m}$  pore size decreases the yield compressive strength of the scaffolds, yet the 500  $\mu\text{m}$  pore-sized scaffolds can also qualify as partial load-bearing implants. Furthermore, the yield strength of this specimen was higher than the compressive strength of cancellous bone and near to the compressive strength of cortical bone, indicating that such scaffolds can be effective in partial load-bearing orthopedic applications, if not in high-stress regions in the body.

However, we did not explore the effect of pore sizes on osteoblast activity and osseointegration in this study. In a follow-up study, we will hypothesize that scaffolds with 300  $\mu\text{m}$  pore size will promote enhanced osseointegration alongside exhibiting robust mechanical properties. Moreover, the effect of 3D printing parameters on the mechanical properties of the porous scaffolds should also be explored as optimization of 3D printing parameters can play a significant role in enhancing the porous scaffolds' mechanical properties.

## **2.4 Conclusion**

In this study, we successfully developed porous PEEK specimens with different pore sizes using an FDM-based 3D printing method. The pore sizes ranged from 100-600  $\mu\text{m}$ , and FDM could print them with precision with no pore-clogging and geometrical inaccuracies. First, we experimentally determined the compressive yield strength and Young's modulus of the porous specimens. The highest compressive yield strength and Young's modulus were recorded to be 41.59 MPa and 791.95 MPa in the case of the printed scaffolds with 300  $\mu\text{m}$  pore size. The scaffolds with 600  $\mu\text{m}$  pore size exhibited the lowest mechanical properties. Subsequently, we used FEA models to analyze the mechanical properties of the porous specimens. The simulations indicated that the stress distribution is highest in the specimen core along the longitudinal infill strands, whereas the outer shell of the specimen experienced a lesser magnitude of stress. The stress distribution increases when the specimen transitions into the inelastic regime. Also, the FEA results indicated that scaffolds with 300  $\mu\text{m}$  pore size exhibited the highest yield strengths. Further, the printed PEEK specimens fail by 2<sup>ND</sup> mode buckling, and the scaffolds with 300  $\mu\text{m}$  pore size can bear as high as 12,870 MPa buckling loads. Thus, our experimental and FEA

results indicate that 3D printed PEEK scaffold with 300  $\mu\text{m}$  pore size is the optimum pore size to yield porous scaffolds with the best mechanical properties for the orthopedic load-bearing application. Increasing the pore size above 300  $\mu\text{m}$  pore will hamper the scaffolds' load-bearing capacity, which is critical in various orthopedic and spine applications.



## CHAPTER III

### Spark Plasma Sintering of Strengthened Amorphous Magnesium Phosphate-Graphene Nano Platelet (AMP-GNP) Bio-Composites for Orthopedic Implants

#### 3.1 Introduction

Synthetic bioceramics are one of the most widely used biomaterials for developing orthopedic implants for treating defects such as hip and knee fractures and diseases like osteoporosis. The prevalent usage of bioceramics as orthopedic implants is for the following reasons. **First**, bioceramics are favorably biocompatible. **Second**, the chemical structure of bioceramics is similar to the inorganic component of bone. **Third**, bioceramics provide various functional groups to the orthopedic implant that help in establishing efficient biochemical interactions with the surrounding tissue and enhance osteoinductance (i.e., inducing bone formation), osteoconductance (i.e., allowing bone-forming cells to move across the implant and slowly replace it with new bone over time, and osteointegration, (i.e., allowing the implant to integrate with the neighboring bone tissue). All such bioceramic properties help promote osteogenesis, i.e., regenerating new healthy bone in the defect area and helping treat bone fractures.

In this regard, the Calcium Phosphate (CaP) family comprises multiple synthetic compounds and is widely used for orthopedic implants. CaPs are among the bioactive compounds that promote osteointegration in orthopedic implants. Specifically, HA and TCP are currently the most used bioceramics in the clinics. However, these synthetic bioceramics have certain limitations. For instance, HA exhibits good bioactive properties, but it has a low degradation rate, limiting its biodegradability *in vivo*. On the other hand,  $\beta$ -TCPs are favorably biodegradable, but it has low osteogenic properties [1]. Moreover, recent studies have shown that CaPs take a prolonged time to regenerate new bone, thus warranting the exploration of other osteogenic materials.

On the contrary, Magnesium Phosphates (MgPs) are the class of bioceramics that have been proven to surpass the osteogenic effects of CaPs. The research in biomedical applications of MgPs is growing rapidly and over the last decade, different MgP compounds such as newberyite, struvite, and tri-magnesium phosphate have served as crucial bioceramic constituents in the development of state-of-the-art implants for orthopedic applications. There are several instances where the inclusion of  $Mg^{2+}$  into CaP compounds has enhanced the bioactivity and osteogenic properties of CaP compounds. Moreover, standalone MgP compounds have been proven to be notably more bioactive and osteogenic than CaPs.

Primarily, there are three important reasons which makes MgPs better than CaPs. First, the dissolution or biodegradation rates of MgPs are higher than those of CaPs [81]. This makes them more apt as biodegradable orthopedic materials with favorable resorption kinetics; (2)  $Mg^{2+}$  ions control several important intracellular activities, and their presence stimulates better bone mineral metabolism (proliferation and differentiation) than CaPs;

and (3)  $Mg^{2+}$  ions inhibit HA crystal growth thus minimizing chances of unwanted crystallization into less soluble mineral phases *in vivo*. One of the most prominent members of the MgP family is the Amorphous Magnesium Phosphates (AMP). This specific MgP phase is well known because AMP is a stable compound and exhibits steady biodegradation kinetics *in vivo* [23, 50, 82, 83]. However, just like any other bioceramic, one of the significant disadvantages of AMPs is their brittleness. To address this limitation, various strategies have been adapted to strengthen MgPs. For example, Carbon-fiber epoxy composites show extremely high modulus and strength in the uniaxial direction. However, they fail relatively under flexural loading due to the weak nature of the interface between the carbon-fiber and epoxy. The desizing and oxidation treatment of carbon fibers and the coating of graphene nano-platelets (GNPs) on the carbon-fibers has been done with an aim to strengthen the interface/interphase between the fiber and the matrix. GNPs were coated on the carbon fibers before making the final laminates through vacuum assisted resin transfer moulding. The flexural strength of the laminates has been found to improve significantly with GNP addition [2]. Graphene, a very recently described material, is an allotrope of carbon which is hexagonal planar 2-dimensional, one atom thick, honeycomb like structure. In other words, graphene is a single layer of graphite, with  $sp^2$  hybridization. From monolayer it can get into bilayer, nanostripes (zig-zag ribbons), grapheme gyroid, box-shaped nanostructure, and arogeel graphene [3]. Its inherent characteristics are from the parental layer of graphite. With high thermal conductance, high strength, nanoparticles of graphene can be used in various industries and applications. Graphene is the thinnest material known and the strongest material ever measured [4] with tensile strength of 130.5 GPa and Young's modulus of 1 TPa. It has been incorporated in CaP scaffolds as graphene-

oxide/magnesium nanohybrids to enhance osteoinductivity [5], reinforced in to hydroxyapatite/ $\beta$ -TCP bioceramics to promote the growth of HA layer on the composite disc [6] With all the above qualities, graphene was shortlisted for creating AMP-GNP composites and study the enhanced mechanical properties as well as the lower corrosiveness alongside maintaining the biological properties of these composites so that the bioactive magnesium phosphate with improved mechanical strength can be adopted for bone repair/osteogenesis.

In this regard, sintering is an important step to consolidate such composites and form the load-bearing scaffolds. Spark plasma sintering (SPS) also known as Field assisted sintering technique (FAST) is a novel consolidation technique suitable to sinter metal, alloys and composites at relatively low temperatures below their melting point and shorter sintering time compared to the conventional techniques. SPS is a newly developed rapid sintering technique with a great potential for achieving fast densification results with minimal grain growth in a short sintering time. It is proven by obtained experimental data that enhanced sinterability of powders subjected to SPS mainly associated with particle surface activation and increased diffusion rates on the contact zones caused by applied pulse current.

Hence, in this study we form nanocomposites out of AMP and GNP first via ball milling and then we use the SPS technique to sinter the samples. We perform through material characterization to analyze the effect of sintering on the AMP-GNP composites. Further, we immerse the samples in Simulated Body Fluid (SBF) to analyze the bioactivity extent of the samples.

## **3.2 Materials and Methods**

### **3.2.1 Raw Material**

Powdered AMP (1-2  $\mu\text{m}$ , 99.9% pure) and graphene nanoplatelets (diameter = 5–10  $\mu\text{m}$ , thickness = 4–20 nm, and number of layers  $\leq 20$ , 99.5% pure) was used as a starting material. AMP was developed using the following protocol. AMP synthesis was carried out in-house, following the ethanol-assisted precipitation method developed by our group. In brief, 11.52 g of magnesium nitrate hexahydrate ( $\text{Mg}(\text{NO}_3)_2 \cdot 6\text{H}_2\text{O}$ , 98% purity, Alfa Aesar, Tewksbury, MA, USA) was added to 100 ml of water and 100 ml of ethanol followed by proper stir mixing. This solution was then added rapidly, at 37°C under constant stirring, to a solution containing 2.97 g of diammonium hydrogen phosphate ( $(\text{NH}_4)_2\text{HPO}_4$ , 99% purity, Fisher Scientific, Hampton, NH, USA) in 250 ml water, 45 ml ammonia (11M) and 295 ml ethanol. The procedure immediately resulted in the formation of precipitate which were collected, centrifuged and washed in ethanol. All the aforementioned steps were carried out within 15 min. Finally, precipitates were placed in an air-drying oven at 60°C overnight to form fine powders.

### **3.2.2 Dry Ball Milling of the AMP-GNP Composites**

The AMP-GNP nanocomposites with varying graphene nanoplatelet content (0.5, 1 wt%) were obtained by first manual mixing and then using the dry ball milling process. The dry ball milling of AMP and GNP mixture was performed in an 80 ml tungsten carbide (WC) jar using 3 mm diameter WC milling balls with the ball to powder weight ratio (BPR) of 10:1 at a milling speed of 200 rpm under argon atmosphere. The ball milling was performed for up to 6 hr with a milling cycle of 10 min followed by 10 min of a pause for cooling to avoid excessive heat generated during ball milling and to prevent cold welding

of the powder. The specimen nomenclature are as follows: AMP (i.e. 100 % bioceramic and 0% GNP), AMP-0.5GNP (AMP with 0.5 wt.% GNP incorporation) and AMP-1GNP (AMP with 1 wt.% GNP incorporation).

### **3.2.3 Spark Plasma Sintering (SPS) of the Nanocomposites**

The AMP and AMP-GNP nanocomposite powders obtained using two different approaches were consolidated using the SPS technique. Cylindrical graphite dies and punches of 10 mm diameter were used for sintering the composite samples. The SPS process was carried out at 600 °C with a heating rate of 100 °C. min<sup>-1</sup> under a uniaxial pressure of 60 MPa and with a holding time of 10 min. This sintering schedule was selected based on prior studies that sintered bioceramics and depending on preliminary studies from our group.

### **3.2.4 Polishing**

The SPS-ed consolidated AMP and AMP-GNP nanocomposite samples were mounted in graphite-based conductive resin, and then the samples were polished sequentially using silicon carbide paper with increasing grit size from 240 to 1200 grit. The final lustrous metallographic finish was obtained after polishing via micro-cloth using 0.04 µm colloidal silica solution and then cleaned in an ultrasonic bath for the metallurgical characterization.

### **3.2.5 Structural Characterization**

X-ray diffraction (XRD) analysis was performed on the specimens to determine the phases present in the AMP-GNP composite specimens. Scanning electron microscopy (SEM) was used to study the structural morphology of the specimens. Two kinds of detectors were used – back scattered SEM and secondary electron detector SEM. Energy

dispersive spectroscopy (EDS) was utilized to identify the elements present in the nanocomposites.

### 3.2.6 SBF Immersion Studies

We used a modified version (t-SBF) of the original Kokubo's composition (c-SBF). The ionic compositions of t-SBF are given in Table 2. AMP (served as control) or AMP-GNP were placed in containers filled with 15 ml t-SBF and kept in a thermostatic water bath (Thermo Scientific) at 37°C for 7 days. t-SBF was replenished every 24 h. Finally, after 7 days, the samples were retrieved, washed, and dried at room temperature prior to further analyses. SEM and EDS were used to study the apatite-forming ability of the AMP-GNP composites. For SEM and EDS, samples were completely dried in an oven, sputtered with gold, and then analyzed in a SEM setup. The weight loss or gain of the AMP-GNP composites (due to SBF immersion) was also monitored over time. 2 samples per group were analyzed for these analyses.

### 3.2.7 Mechanical Property Characterization

Vickers Microhardness was determined using Wilson VH1202 hardness tester from Buehler having an accuracy of  $\pm 1.5\%$ . Microhardness was evaluated under test force of 0.5 kgf and dwell time of 10 seconds as recommended by ASTM E384 standards. A pyramid shaped diamond indenter was used for indentation. Indent diagonals were measured using the measurement system in the Wilson DiaMet and the Vickers microhardness number was calculated for the load and indent dimensions.

Vickers hardness number (VHN) is calculated using equation mentioned below,

$$VHN = 2P \sin\left(\frac{\alpha}{2}\right) = 1.854P/d^2$$

Where,  $P$  is the test force in gram-force,  $d$  is the average of the diagonals if the indentation in  $\mu\text{m}$ ,  $\alpha$  is the indenter tip angle which is taken as  $136^\circ$ .

The test was carried out according to ASTM E384 standards. Test was performed under ambient conditions and at least ten readings at different position were taken for each sample.

### 3.3 Results and Discussion

#### 3.3.1 Physical Characterization

The digital images of the pristine AMP and nanocomposite powders are shown in **Figure 3.1**. It can be seen that the pristine AMP powders were white in color. As opposed, the AMP-0.5 GNP exhibited a light grey in color indicating the presence or the incorporation of the GNP. Furthermore, the AMP-1GNP exhibited a dark black color (as compared to the AMP-0.5 GNP) which indicates that this composition has higher degrees of GNP presence in it. Overall, the powders exhibited a homogenous color distribution of either light gray or black. Thus, the qualitative analysis indicates that the dry ball milling was useful to form a homogeneous mixture of AMP-GNP nanocomposites with varying GNP incorporation extent.

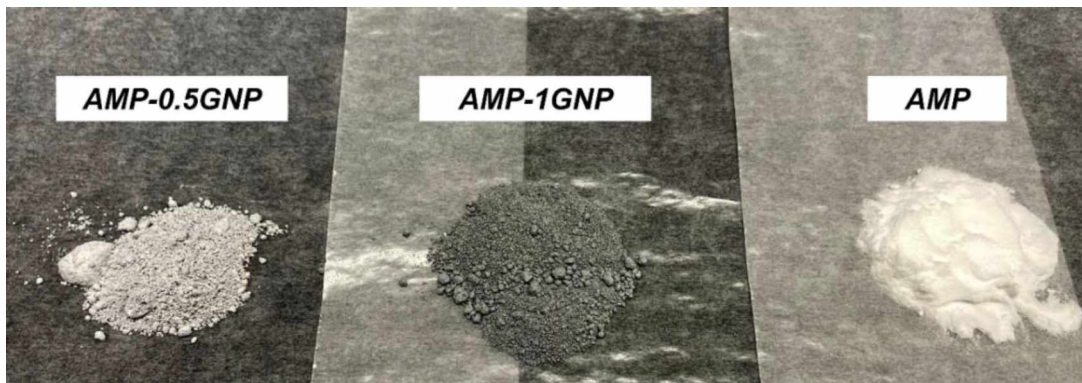


**Figure 3.1:** Digital photographs of the pristine AMP and AMP with varying GNP (0.5 and 1 wt.%) after dry ball milling.



The **Figure 3.2** shows the digital images of the SPS-ed specimens. The SPS-ed AMP pellet broke into pieces when it was retrieved from the graphite die, indicating that the sintered AMP was extremely brittle in nature. This is expected as bioceramics are inherently brittle in nature. On the contrary, AMP-0.5GNP and AMP-1GNP did not break after it was retrieved from the die. Instead, the composite samples exhibited a strong, firm and consolidated structure. The composite specimen pellets were compact in nature and can be handled easily unlike the brittle AMP pellets.

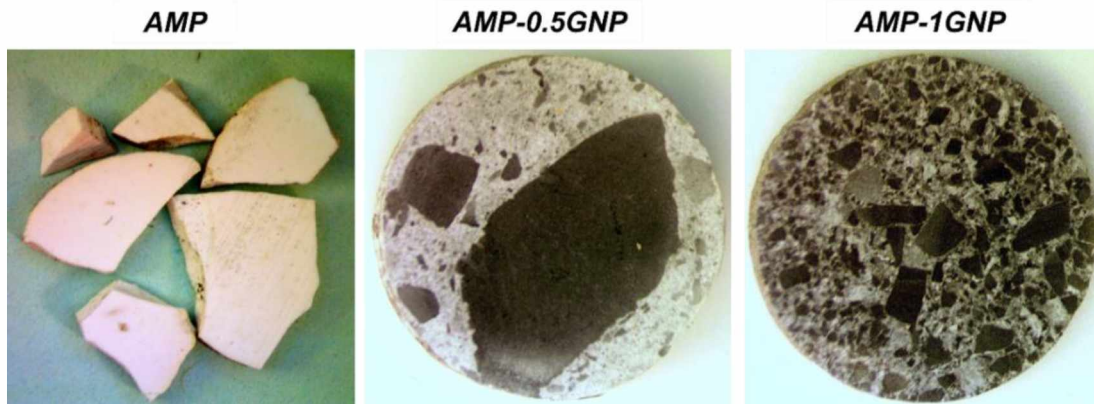


**Figure 3.2:** Digital photographs of the sintered i.e., SPS-ed AMP and AMP with varying GNP (0.5 and 1 wt.%). It is evident that the sintered AMP was extremely brittle that it broke when it was retrieved from the holder. On the contrary the AMP-0.5 GNP and AMP-1GNP specimens were intact exhibiting low brittleness and high toughness.

The **Figure 3.3** shows the XRD plots of the AMP and AMP-GNP composites. All the diffraction plots correspond to farringtonite ( $\text{Mg}_3(\text{PO}_4)_2$ , PDF: 98-001-4443) with small traces of periclase ( $\text{MgO}$ , PDF: 98-000-0349, 98-000-5719). Very few diffraction peaks for both phases were detected with broadened nature and significantly low intensity. Additionally, the wide hump pertaining to the amorphous nature (i.e., for AMP) was not present. Heat-treating or sintering AMP at  $600^\circ\text{C}$  resulted in the formation of single-phasic and highly crystalline farringtonite, as indicated by well-defined and sharp diffraction patterns. However, XRD did not detect any diffraction peaks of GNPs in the AMP

specimen. The peak corresponding to HCP (0002) carbon should be visible in the AMP-1GNP composites. However, this (0002) carbon peak associated with graphite has not been observed in other AMP-GNP composites due to the relatively lower content ( $\leq 1$  wt%) of GNP concentration, which is beyond the detectable limit of XRD. Furthermore, the XRD plots indicated that there was no reaction between the AMP and GNP during the sintering process as no impurities and secondary phases were formed.

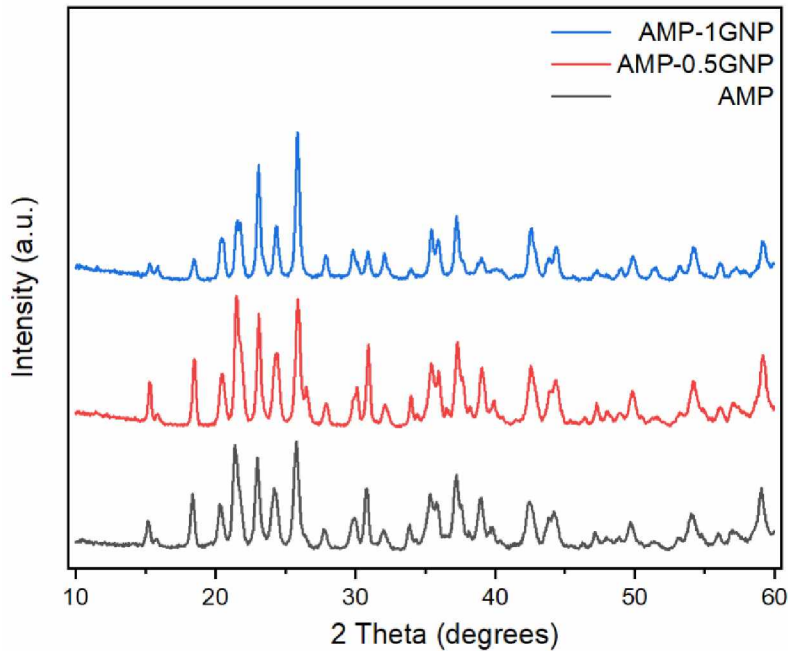


**Figure 3.3:** X-ray diffraction of the nanocomposite powders. All the diffraction plots correspond to farringtonite ( $\text{Mg}_3(\text{PO}_4)_2$ , PDF: 98-001-4443).

The **Figure 3.4** shows the SEM analysis of the SPS-ed composites and the pristine AMP. SEM images presented in case of the AMP reveal the morphology of the sintered AMP. The images denote the presence of spherical particles either individually or coalesced with randomly orientated and stacked sheets. In some regions heat-treatments resulted in the separation of those unified clusters into individual structures with sharper

boundaries. Moreover, in certain regions, the spherical particle morphology of the AMPs were distinct in the micrographs (Figure 3.5).

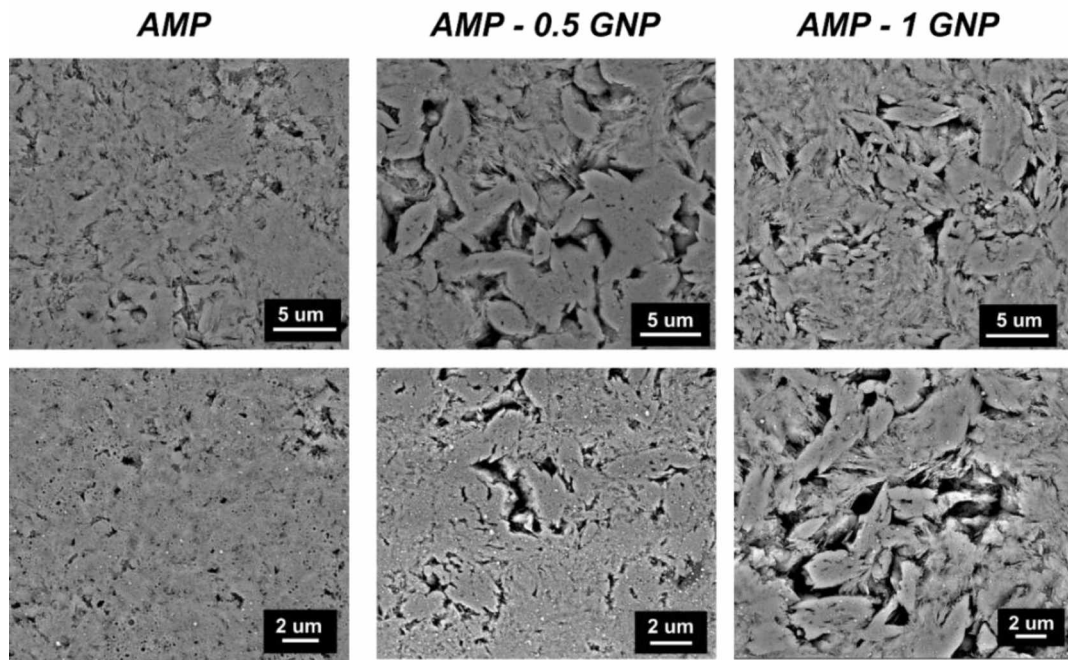


**Figure 3.4:** Back scattered-Scanning electron microscopy (BS-SEM) analysis of the SPS-ed AMP and AMP-GNP specimens.

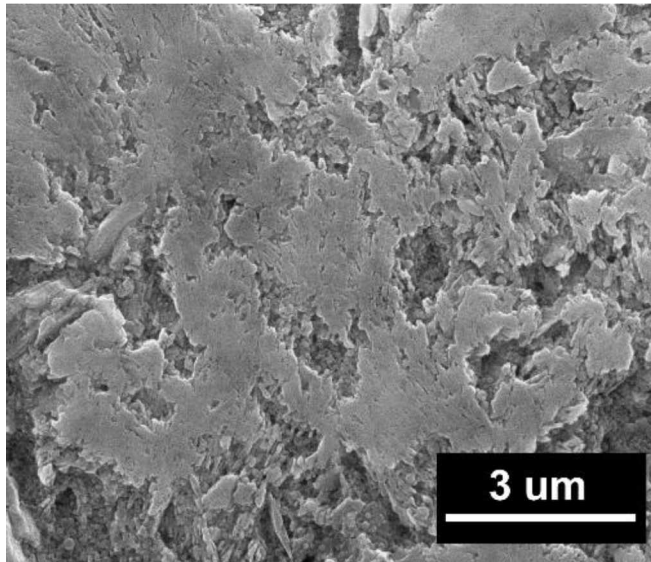


**Figure 3.5:** High magnification SEM image (secondary electron detector) showing the porous structure on the top surface of a sintered AMP scaffold. The spherical particles of the sintered AMP can be seen.

### 3.3.2 SBF Immersion Studies

The bioactivity of the composites were assessed *in vitro* by SBF immersion for 7 days and the results are presented in **Figure 3.6**. In all the specimens thick amount of apatite formation was observed. The apatite formation on the specimen was characterized by the globules deposited on the specimen surface. It is evident from the micrographs that the globules entirely cover the specimen surface at the end of the immersion period. When inspected closely, the globules consist of flake-like morphology which is the signature morphology of the apatite. Moreover, a thick layer of apatite with cracks were also formed. Interestingly, apart from the apatite globules, flower-like architecture particles were also formed on the specimens as a result of the SBF immersion. The micron-sized flower like particles represent that many crystals arranged in the orientation of flower. The longitudinal particles or rods arranged in a manner such that one end of the rods are fixed at the center of the flower-like architecture. These particles are the signature signs of magnesium phosphates, which indicates that the SBF immersion also resulted in forming further magnesium phosphate particles other than AMP. The results are further corroborated by the EDS analysis. The EDS analysis of the flower-like particles show a high concentration of Mg, whereas the EDS of the apatite globules show a high concentration of Ca and no presence of Mg. This is indeed interesting because SBF immersion of the nanocomposites and the AMP resulted in two different prominent structures – one which is rich in calcium which is important for osseointegration, and bone formation and the other structure is rich in Mg which helps in stabilizing the dissolution kinetics of the nanocomposites. The latter feature is important because we do not want a fast dissolution kinetics of the samples as these will be used as load bearing scaffolds. Thus, the presence of Mg would stabilize the

dissolution mechanisms of the scaffolds. This is further corroborated by the weight analysis studies (**Figure 3.7**). We first hypothesized that the scaffolds will degrade over time in SBF but our hypothesis was proven incorrect. Instead, we noticed that the composites gained weight with the highest being in pristine SPS-ed AMP. This is because AMP is one of the most stable phase and it helped in forming significantly more apatite and additional MgP particles on itself which resulted in a good increase in weight. On the contrary, the composite scaffolds did not gain as much weight as the AMP because the amount of apatite or other MgP phases was less. However, they did not degrade over time and both the AMP 0.5 GNP and AMP-1GNP exhibited favorable bioactivity by virtue of the high amount of apatite that was formed on the specimens.

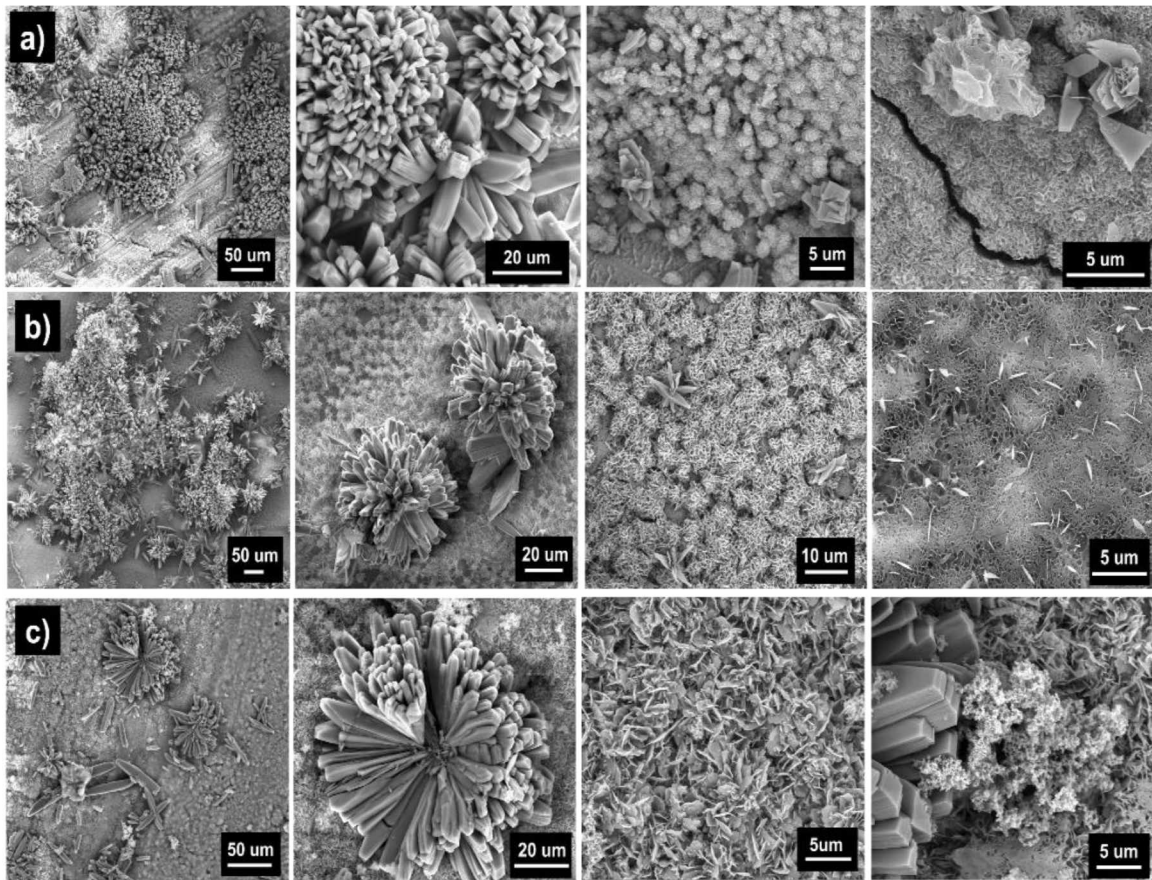


**Figure 3.6:** SEM images of the specimen surface after SBF immersion for 7 days.

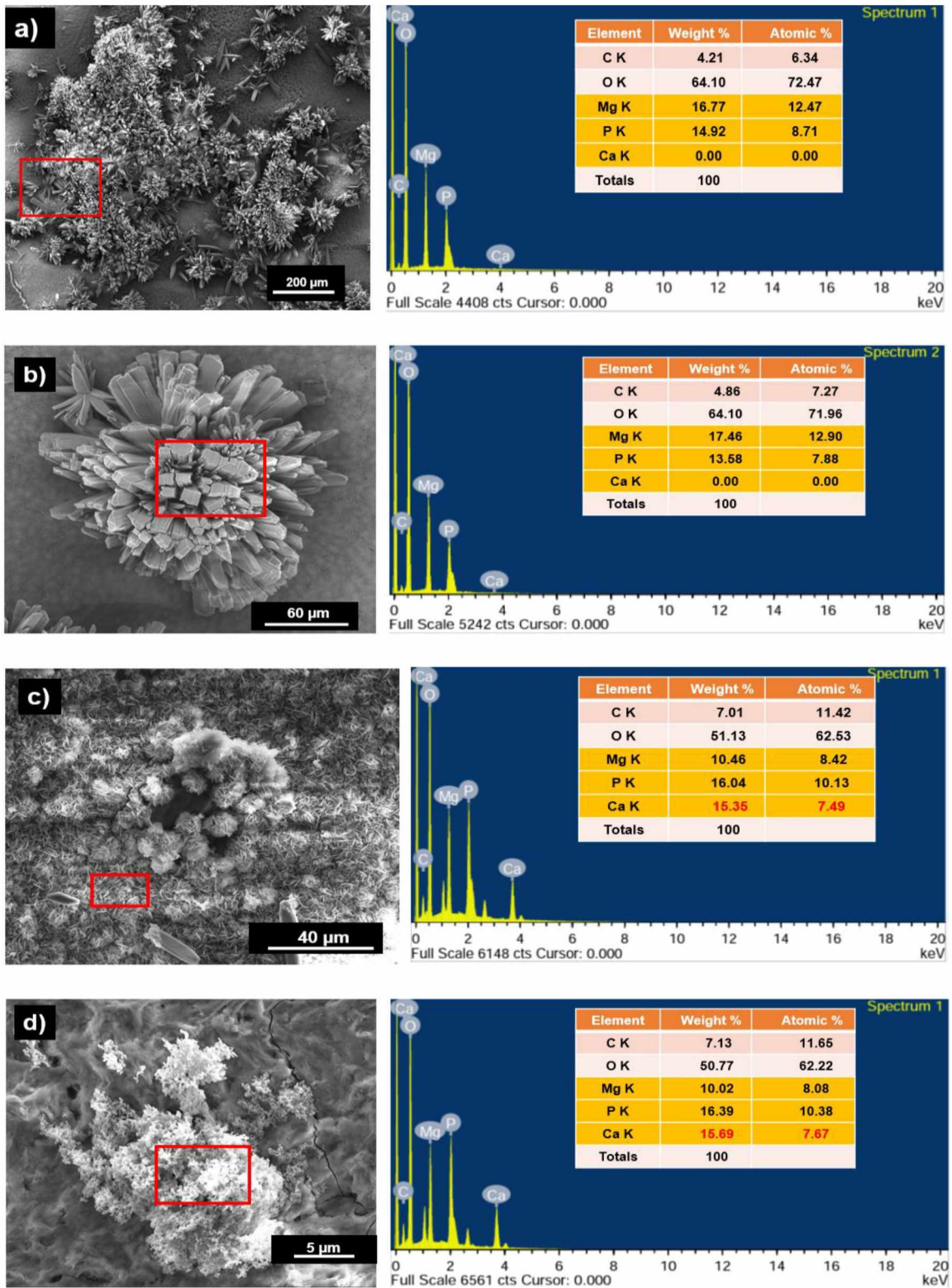
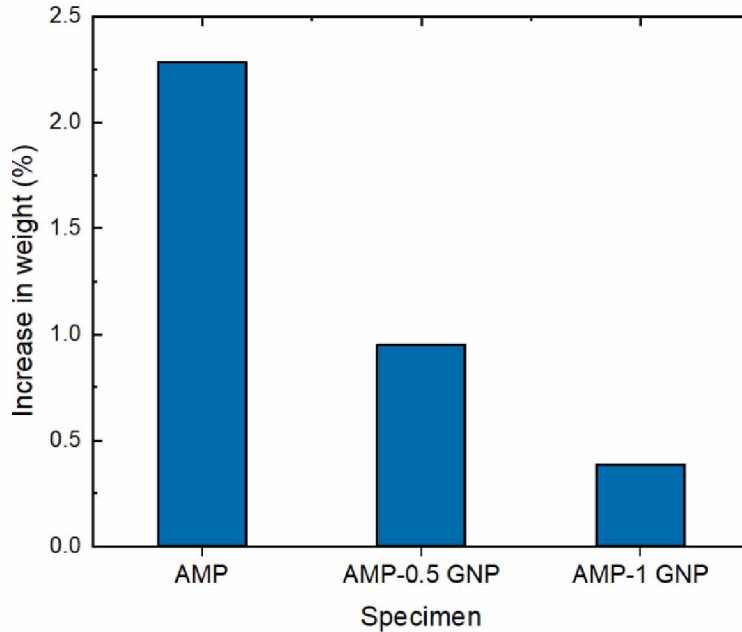


Figure 3.7: EDS analysis of SBF immersed specimens.



**Figure 3.8:** Weight gain analysis of the specimens after immersing in SBF for 7 days.

### 3.3.3 Mechanical Property Analysis

Vickers microhardness of SPS processed AMP-GNP composites. It is observed that the microhardness drastically increased due to addition of GNP reinforcement in AMP matrix as compared with pure AMP depicting hardness value of 61.1 VHN. It can be attributed to the clean interfacial bond, refined size, uniformity, and interfacial strength of in situ formed in AMP particulates. 1GNP exhibited the highest hardness value of 69.2 VHN. AMP-GNP composite, this can be attributed to presence is mainly due to high volume fraction.

From the **Figure 3.9**, it is evident that adding the GNP by weight enhances the hardness property of the AMP. The least hardness was seen in the case of Raw AMP, while maximum hardness was seen in case of 1 GNP-AMP composite.

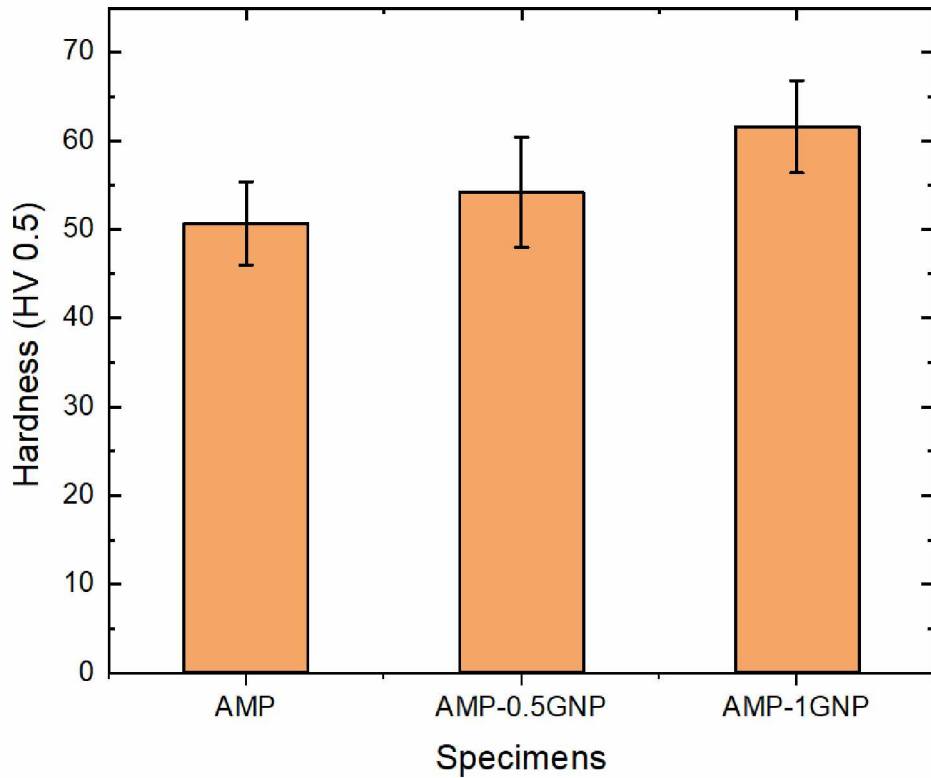


**Figure 3.9:** Hardness test.

### 3.4 Conclusion

With the help of this study, I confirm that AMP-GNP nanocomposites can be formed effectively and most importantly the SPS technique is an efficient tool to form highly compact and firm scaffolds. Our physical characterization analysis did not identify the GNP in the AMP matrix, but qualitative analysis indicated that the AMP-GNP composites can be formed homogenously using the ball milling and SPS technique. Our bioactivity analysis indicated that the AMP-GNP composites are highly bioactive in nature, and they do not degrade very easily which is preferred in load-bearing scaffolds. Further studies are required to analyze the mechanical properties of these AMP-GNP scaffolds. Also, through in vitro studies will be required to analyze the effect of osteoblasts on such scaffolds.



## REFERENCES

### Chapter I

- [1] R.B. Rigby, Polyetheretherketone, Engineering thermoplastics, CRC Press2020, pp. 299-314.
- [2] S.J. Park, J.E. Lee, J. Park, N.-K. Lee, Y. Son, S.-H. Park, High-temperature 3D printing of polyetheretherketone products: Perspective on industrial manufacturing applications of super engineering plastics, *Materials & Design* 211 (2021) 110163.
- [3] I.V. Panayotov, V. Orti, F. Cuisinier, J. Yachouh, Polyetheretherketone (PEEK) for medical applications, *Journal of Materials Science: Materials in Medicine* 27(7) (2016) 1-11.
- [4] S.M. Kurtz, J.N. Devine, PEEK biomaterials in trauma, orthopedic, and spinal implants, *Biomaterials* 28(32) (2007) 4845-4869.
- [5] K. Elhatab, P. Sikder, J.M. Walker, M.C. Bottino, S.B. Bhaduri, Fabrication and evaluation of 3-D printed PEEK scaffolds containing Macropores by design, *Materials Letters* 263 (2020) 127227.
- [6] B. Berman, 3-D printing: The new industrial revolution, *Business horizons* 55(2) (2012) 155-162.
- [7] M. Schmidt, D. Pohle, T. Rechtenwald, Selective laser sintering of PEEK, *CIRP annals* 56(1) (2007) 205-208.
- [8] D.L. Bourell, T.J. Watt, D.K. Leigh, B. Fulcher, Performance limitations in polymer laser sintering, *Physics Procedia* 56 (2014) 147-156.

- [9] K. Elhatab, M.S. Hefzy, Z. Hanf, B. Crosby, A. Enders, T. Smiczek, M. Haghshenas, A. Jahadakbar, M. Elahinia, Biomechanics of Additively Manufactured Metallic Scaffolds—A Review, *Materials* 14(22) (2021) 6833.
- [10] X. Han, D. Yang, C. Yang, S. Spintzyk, L. Scheideler, P. Li, D. Li, J. Geis-Gerstorfer, F. Rupp, Carbon fiber reinforced PEEK composites based on 3D-printing technology for orthopedic and dental applications, *Journal of clinical medicine* 8(2) (2019) 240.
- [11] B.I. Oladapo, S.O. Ismail, O.K. Bowoto, F.T. Omigbodun, M.A. Olawumi, M.A. Muhammad, Lattice design and 3D-printing of PEEK with  $\text{Ca}_{10}(\text{OH})(\text{PO}_4)_3$  and in-vitro bio-composite for bone implant, *International Journal of Biological Macromolecules* 165 (2020) 50-62.
- [12] K. Elhatab, S.B. Bhaduri, J.G. Lawrence, P. Sikder, Fused Filament Fabrication (Three-Dimensional Printing) of Amorphous Magnesium Phosphate/Poly(lactic Acid) Macroporous Biocomposite Scaffolds, *ACS Applied Bio Materials* 4(4) (2021) 3276-3286.
- [13] W.Z. Wu, P. Geng, J. Zhao, Y. Zhang, D.W. Rosen, H.B. Zhang, Manufacture and thermal deformation analysis of semicrystalline polymer polyether ether ketone by 3D printing, *Materials Research Innovations* 18(sup5) (2014) S5-12.
- [14] B. Valentan, Ž. Kadivnik, T. Brajljih, A. Anderson, I. Drstvenšek, Processing poly(ether etherketone) on a 3D printer for thermoplastic modelling, *Materiali in tehnologije* 47(6) (2013) 715-721.

- [15] W.Z. Wu, P. Geng, J. Zhao, Y. Zhang, D.W. Rosen, H.B. Zhang, Manufacture and thermal deformation analysis of semicrystalline polymer polyether ether ketone by 3D printing, *Materials Research Innovations* 18(sup5) (2014) S5-12-S5-16.
- [16] W. Wu, P. Geng, G. Li, D. Zhao, H. Zhang, J. Zhao, Influence of layer thickness and raster angle on the mechanical properties of 3D-printed PEEK and a comparative mechanical study between PEEK and ABS, *Materials* 8(9) (2015) 5834-5846.
- [17] M. Vaezi, S. Yang, Extrusion-based additive manufacturing of PEEK for biomedical applications, *Virtual and Physical Prototyping* 10(3) (2015) 123-135.
- [18] C. Yang, X. Tian, D. Li, Y. Cao, F. Zhao, C. Shi, Influence of thermal processing conditions in 3D printing on the crystallinity and mechanical properties of PEEK material, *Journal of Materials Processing Technology* 248 (2017) 1-7.
- [19] P. Wang, B. Zou, H. Xiao, S. Ding, C. Huang, Effects of printing parameters of fused deposition modeling on mechanical properties, surface quality, and microstructure of PEEK, *Journal of Materials Processing Technology* 271 (2019) 62-74.
- [20] Y. Wang, W.-D. Müller, A. Rumjahn, A. Schwitalla, Parameters influencing the outcome of additive manufacturing of tiny medical devices based on PEEK, *Materials* 13(2) (2020) 466.
- [21] F. Zhao, D. Li, Z. Jin, Preliminary investigation of poly-ether-ether-ketone based on fused deposition modeling for medical applications, *Materials* 11(2) (2018) 288.
- [22] P. Sikder, J.A. Ferreira, E.A. Fakhrabadi, K.Z. Kantorski, M.W. Liberatore, M.C. Bottino, S.B. Bhaduri, Bioactive amorphous magnesium phosphate-

- polyetheretherketone composite filaments for 3D printing, *Dental Materials* 36(7) (2020) 865-883.
- [23] A. Standard, D695: Standard test method for compressive properties of rigid plastics, ASTM International, West Conchohocken (2008).
- [24] U.E. Iso, *Plastics-Determination of tensile properties-Part 2: Test conditions for moulding and extrusion plastics*, International Organization for Standardization: Switzerland (2012).
- [25] X. Deng, Z. Zeng, B. Peng, S. Yan, W. Ke, Mechanical properties optimization of poly-ether-ether-ketone via fused deposition modeling, *Materials* 11(2) (2018) 216.
- [26] M. Mrówka, T. Machoczek, P. Jureczko, K. Jozsko, M. Gzik, W. Wolański, K. Wilk, Mechanical, Chemical, and Processing Properties of Specimens Manufactured from Poly-Ether-Ether-Ketone (PEEK) Using 3D Printing, *Materials* 14(11) (2021) 2717.
- [27] J.E. Mark, *Physical properties of polymers handbook*, Springer2007.
- [28] D.J. Jaekel, D.W. MacDonald, S.M. Kurtz, Characterization of PEEK biomaterials using the small punch test, *Journal of the mechanical behavior of biomedical materials* 4(7) (2011) 1275-1282.
- [29] P.J. Rae, E.N. Brown, E.B. Orlor, The mechanical properties of poly (ether-ether-ketone)(PEEK) with emphasis on the large compressive strain response, *Polymer* 48(2) (2007) 598-615.
- [30] S. Ding, B. Zou, P. Wang, H. Ding, Effects of nozzle temperature and building orientation on mechanical properties and microstructure of PEEK and PEI printed by 3D-FDM, *Polymer Testing* 78 (2019) 105948.

- [31] M. Zalaznik, M. Kalin, S. Novak, Influence of the processing temperature on the tribological and mechanical properties of poly-ether-ether-ketone (PEEK) polymer, *Tribology International* 94 (2016) 92-97.
- [32] A.R. Zanjanijam, I. Major, J.G. Lyons, U. Lafont, D.M. Devine, Fused filament fabrication of peek: A review of process-structure-property relationships, *Polymers* 12(8) (2020) 1665.
- [33] Y. Wang, W.-D. Müller, A. Rumjahn, F. Schmidt, A.D. Schwitalla, Mechanical properties of fused filament fabricated PEEK for biomedical applications depending on additive manufacturing parameters, *journal of the mechanical behavior of biomedical materials* 115 (2021) 104250.
- [34] B. Hu, X. Duan, Z. Xing, Z. Xu, C. Du, H. Zhou, R. Chen, B. Shan, Improved design of fused deposition modeling equipment for 3D printing of high-performance PEEK parts, *Mechanics of Materials* 137 (2019) 103139.
- [35] S.M. Kurtz, An overview of PEEK biomaterials, *PEEK biomaterials handbook* (2019) 3-9.
- [36] D. Fischer, C. Eßbach, R. Schönherr, D. Dietrich, D. Nickel, Improving inner structure and properties of additive manufactured amorphous plastic parts: the effects of extrusion nozzle diameter and layer height, *Additive Manufacturing* (2022) 102596.
- [37] C.-Y. Liaw, J.W. Tolbert, L.W. Chow, M. Guvendiren, Interlayer bonding strength of 3D printed PEEK specimens, *Soft Matter* 17(18) (2021) 4775-4789.

- [38] P. Geng, J. Zhao, W. Wu, W. Ye, Y. Wang, S. Wang, S. Zhang, Effects of extrusion speed and printing speed on the 3D printing stability of extruded PEEK filament, *Journal of Manufacturing Processes* 37 (2019) 266-273.

## **Chapter II**

- [1] R.B. Rigby, Polyetheretherketone, *Engineering thermoplastics*, CRC Press 2020, pp. 299-314.
- [2] S.J. Park, J.E. Lee, J. Park, N.-K. Lee, Y. Son, S.-H. Park, High-temperature 3D printing of polyetheretherketone products: Perspective on industrial manufacturing applications of super engineering plastics, *Materials & Design* 211 (2021) 110163.
- [3] I.V. Panayotov, V. Orti, F. Cuisinier, J. Yachouh, Polyetheretherketone (PEEK) for medical applications, *Journal of Materials Science: Materials in Medicine* 27(7) (2016) 1-11.
- [4] S.M. Kurtz, J.N. Devine, PEEK biomaterials in trauma, orthopedic, and spinal implants, *Biomaterials* 28(32) (2007) 4845-4869.
- [5] K. Elhatab, P. Sikder, J.M. Walker, M.C. Bottino, S.B. Bhaduri, Fabrication and evaluation of 3-D printed PEEK scaffolds containing Macropores by design, *Materials Letters* 263 (2020) 127227.
- [6] B. Berman, 3-D printing: The new industrial revolution, *Business horizons* 55(2) (2012) 155-162.
- [7] M. Schmidt, D. Pohle, T. Rechtenwald, Selective laser sintering of PEEK, *CIRP annals* 56(1) (2007) 205-208.
- [8] D.L. Bourell, T.J. Watt, D.K. Leigh, B. Fulcher, Performance limitations in polymer laser sintering, *Physics Procedia* 56 (2014) 147-156.

- [9] K. Elhatab, M.S. Hefzy, Z. Hanf, B. Crosby, A. Enders, T. Smiczek, M. Haghshenas, A. Jahadakbar, M. Elahinia, Biomechanics of Additively Manufactured Metallic Scaffolds—A Review, *Materials* 14(22) (2021) 6833.
- [10] X. Han, D. Yang, C. Yang, S. Spintzyk, L. Scheideler, P. Li, D. Li, J. Geis-Gerstorfer, F. Rupp, Carbon fiber reinforced PEEK composites based on 3D-printing technology for orthopedic and dental applications, *Journal of clinical medicine* 8(2) (2019) 240.
- [11] B.I. Oladapo, S.O. Ismail, O.K. Bowoto, F.T. Omigbodun, M.A. Olawumi, M.A. Muhammad, Lattice design and 3D-printing of PEEK with  $\text{Ca}_{10}(\text{OH})(\text{PO}_4)_3$  and in-vitro bio-composite for bone implant, *International Journal of Biological Macromolecules* 165 (2020) 50-62.
- [12] K. Elhatab, S.B. Bhaduri, J.G. Lawrence, P. Sikder, Fused Filament Fabrication (Three-Dimensional Printing) of Amorphous Magnesium Phosphate/Poly(lactic Acid) Macroporous Biocomposite Scaffolds, *ACS Applied Bio Materials* 4(4) (2021) 3276-3286.
- [13] W.Z. Wu, P. Geng, J. Zhao, Y. Zhang, D.W. Rosen, H.B. Zhang, Manufacture and thermal deformation analysis of semicrystalline polymer polyether ether ketone by 3D printing, *Materials Research Innovations* 18(sup5) (2014) S5-12.
- [14] B. Valentan, Ž. Kadivnik, T. Brajljih, A. Anderson, I. Drstvenšek, Processing poly(ether etherketone) on a 3D printer for thermoplastic modelling, *Materiali in tehnologije* 47(6) (2013) 715-721.

- [15] W.Z. Wu, P. Geng, J. Zhao, Y. Zhang, D.W. Rosen, H.B. Zhang, Manufacture and thermal deformation analysis of semicrystalline polymer polyether ether ketone by 3D printing, *Materials Research Innovations* 18(sup5) (2014) S5-12-S5-16.
- [16] W. Wu, P. Geng, G. Li, D. Zhao, H. Zhang, J. Zhao, Influence of layer thickness and raster angle on the mechanical properties of 3D-printed PEEK and a comparative mechanical study between PEEK and ABS, *Materials* 8(9) (2015) 5834-5846.
- [17] M. Vaezi, S. Yang, Extrusion-based additive manufacturing of PEEK for biomedical applications, *Virtual and Physical Prototyping* 10(3) (2015) 123-135.
- [18] C. Yang, X. Tian, D. Li, Y. Cao, F. Zhao, C. Shi, Influence of thermal processing conditions in 3D printing on the crystallinity and mechanical properties of PEEK material, *Journal of Materials Processing Technology* 248 (2017) 1-7.
- [19] P. Wang, B. Zou, H. Xiao, S. Ding, C. Huang, Effects of printing parameters of fused deposition modeling on mechanical properties, surface quality, and microstructure of PEEK, *Journal of Materials Processing Technology* 271 (2019) 62-74.
- [20] Y. Wang, W.-D. Müller, A. Rumjahn, A. Schwitalla, Parameters influencing the outcome of additive manufacturing of tiny medical devices based on PEEK, *Materials* 13(2) (2020) 466.
- [21] P. Sikder, B.T. Challa, S.K. Gummadi, A Comprehensive Analysis on the Processing-Structure-Property Relationships of FDM-based 3-D Printed Polyetheretherketone (PEEK) Structures, *Materialia* (2022) 101427.



- [22] F. Zhao, D. Li, Z. Jin, Preliminary investigation of poly-ether-ether-ketone based on fused deposition modeling for medical applications, *Materials* 11(2) (2018) 288.
- [23] P. Sikder, J.A. Ferreira, E.A. Fakhrabadi, K.Z. Kantorski, M.W. Liberatore, M.C. Bottino, S.B. Bhaduri, Bioactive amorphous magnesium phosphate-polyetheretherketone composite filaments for 3D printing, *Dental Materials* 36(7) (2020) 865-883.
- [24] A. Standard, D695: Standard test method for compressive properties of rigid plastics, ASTM International, West Conchohocken (2008).
- [25] U.E. Iso, Plastics-Determination of tensile properties-Part 2: Test conditions for moulding and extrusion plastics, International Organization for Standardization: Switzerland (2012).
- [26] X. Deng, Z. Zeng, B. Peng, S. Yan, W. Ke, Mechanical properties optimization of poly-ether-ether-ketone via fused deposition modeling, *Materials* 11(2) (2018) 216.
- [27] M. Mrówka, T. Machoczek, P. Jureczko, K. Jozsko, M. Gzik, W. Wolański, K. Wilk, Mechanical, Chemical, and Processing Properties of Specimens Manufactured from Poly-Ether-Ether-Ketone (PEEK) Using 3D Printing, *Materials* 14(11) (2021) 2717.
- [28] J.E. Mark, Physical properties of polymers handbook, Springer2007.
- [29] D.J. Jaekel, D.W. MacDonald, S.M. Kurtz, Characterization of PEEK biomaterials using the small punch test, *Journal of the mechanical behavior of biomedical materials* 4(7) (2011) 1275-1282.

- [30] P.J. Rae, E.N. Brown, E.B. Orlor, The mechanical properties of poly (ether-ether-ketone)(PEEK) with emphasis on the large compressive strain response, *Polymer* 48(2) (2007) 598-615.
- [31] S. Ding, B. Zou, P. Wang, H. Ding, Effects of nozzle temperature and building orientation on mechanical properties and microstructure of PEEK and PEI printed by 3D-FDM, *Polymer Testing* 78 (2019) 105948.
- [32] M. Zalaznik, M. Kalin, S. Novak, Influence of the processing temperature on the tribological and mechanical properties of poly-ether-ether-ketone (PEEK) polymer, *Tribology International* 94 (2016) 92-97.
- [33] A.R. Zanjanijam, I. Major, J.G. Lyons, U. Lafont, D.M. Devine, Fused filament fabrication of peek: A review of process-structure-property relationships, *Polymers* 12(8) (2020) 1665.
- [34] Y. Wang, W.-D. Müller, A. Rumjahn, F. Schmidt, A.D. Schwitalla, Mechanical properties of fused filament fabricated PEEK for biomedical applications depending on additive manufacturing parameters, *journal of the mechanical behavior of biomedical materials* 115 (2021) 104250.
- [35] B. Hu, X. Duan, Z. Xing, Z. Xu, C. Du, H. Zhou, R. Chen, B. Shan, Improved design of fused deposition modeling equipment for 3D printing of high-performance PEEK parts, *Mechanics of Materials* 137 (2019) 103139.
- [36] S.M. Kurtz, An overview of PEEK biomaterials, *PEEK biomaterials handbook* (2019) 3-9.
- [37] D. Fischer, C. Eßbach, R. Schönherr, D. Dietrich, D. Nickel, Improving inner structure and properties of additive manufactured amorphous plastic parts: the

- effects of extrusion nozzle diameter and layer height, *Additive Manufacturing* (2022) 102596.
- [38] C.-Y. Liaw, J.W. Tolbert, L.W. Chow, M. Guvendiren, Interlayer bonding strength of 3D printed PEEK specimens, *Soft Matter* 17(18) (2021) 4775-4789.
- [39] P. Geng, J. Zhao, W. Wu, W. Ye, Y. Wang, S. Wang, S. Zhang, Effects of extrusion speed and printing speed on the 3D printing stability of extruded PEEK filament, *Journal of Manufacturing Processes* 37 (2019) 266-273.
- [40] J.B. Rose, Discovery and development of the “Vicatex” Polyaryletherketone PEEK, *High performance polymers: their origin and development*, Springer 1986, pp. 187-193.
- [41] J.-H. Chen, C. Liu, L. You, C.A. Simmons, Boning up on Wolff's Law: mechanical regulation of the cells that make and maintain bone, *Journal of biomechanics* 43(1) (2010) 108-118.
- [42] M. Niinomi, Mechanical properties of biomedical titanium alloys, *Materials Science and Engineering: A* 243(1-2) (1998) 231-236.
- [43] Y. Noyama, T. Miura, T. Ishimoto, T. Itaya, M. Niinomi, T. Nakano, Bone loss and reduced bone quality of the human femur after total hip arthroplasty under stress-shielding effects by titanium-based implant, *Materials transactions* 53(3) (2012) 565-570.
- [44] W.T. Lee, J.Y. Koak, Y.J. Lim, S.K. Kim, H.B. Kwon, M.J. Kim, Stress shielding and fatigue limits of poly-ether-ether-ketone dental implants, *Journal of Biomedical Materials Research Part B: Applied Biomaterials* 100(4) (2012) 1044-1052.

- [45] A. Alnazzawi, Effect of fixed metallic oral appliances on oral health, *Journal of International Society of Preventive & Community Dentistry* 8(2) (2018) 93.
- [46] B. Di Maggio, P. Sessa, P. Mantelli, P. Maniscalco, F. Rivera, G.M. Calori, L. Bisogno, G. Scaravilli, M. Caforio, PEEK radiolucent plate for distal radius fractures: multicentre clinical results at 12 months follow up, *Injury* 48 (2017) S34-S38.
- [47] S. Najeeb, Z. Khurshid, J.P. Matinlinna, F. Siddiqui, M.Z. Nassani, K. Baroudi, Nanomodified peek dental implants: Bioactive composites and surface modification—A review, *International journal of dentistry* 2015 (2015).
- [48] F. Rahmitasari, Y. Ishida, K. Kurahashi, T. Matsuda, M. Watanabe, T. Ichikawa, PEEK with reinforced materials and modifications for dental implant applications, *Dentistry journal* 5(4) (2017) 35.
- [49] Y. Ren, P. Sikder, B. Lin, S.B. Bhaduri, Microwave assisted coating of bioactive amorphous magnesium phosphate (AMP) on polyetheretherketone (PEEK), *Materials Science and Engineering: C* 85 (2018) 107-113.
- [50] P. Sikder, C.R. Grice, B. Lin, V.K. Goel, S.B. Bhaduri, Single-phase, antibacterial trimagnesium phosphate hydrate coatings on polyetheretherketone (PEEK) implants by rapid microwave irradiation technique, *ACS Biomaterials Science & Engineering* 4(8) (2018) 2767-2783.
- [51] J.H. Lee, H.L. Jang, K.M. Lee, H.-R. Baek, K. Jin, K.S. Hong, J.H. Noh, H.-K. Lee, In vitro and in vivo evaluation of the bioactivity of hydroxyapatite-coated polyetheretherketone biocomposites created by cold spray technology, *Acta biomaterialia* 9(4) (2013) 6177-6187.

- [52] S. Stübinger, A. Drechsler, A. Bürki, K. Klein, P. Kronen, B. von Rechenberg, Titanium and hydroxyapatite coating of polyetheretherketone and carbon fiber-reinforced polyetheretherketone: A pilot study in sheep, *Journal of Biomedical Materials Research Part B: Applied Biomaterials* 104(6) (2016) 1182-1191.
- [53] W. Wang, C.J. Luo, J. Huang, M. Edirisinghe, PEEK surface modification by fast ambient-temperature sulfonation for bone implant applications, *Journal of the Royal Society Interface* 16(152) (2019) 20180955.
- [54] H. Zhou, V.K. Goel, S.B. Bhaduri, A fast route to modify biopolymer surface: a study on polyetheretherketone (PEEK), *Materials Letters* 125 (2014) 96-98.
- [55] K. Gan, H. Liu, L. Jiang, X. Liu, X. Song, D. Niu, T. Chen, C. Liu, Bioactivity and antibacterial effect of nitrogen plasma immersion ion implantation on polyetheretherketone, *Dental Materials* 32(11) (2016) e263-e274.
- [56] D. Briem, S. Strametz, K. Schröder, N.M. Meenen, W. Lehmann, W. Linhart, A. Ohl, J.M. Rueger, Response of primary fibroblasts and osteoblasts to plasma treated polyetheretherketone (PEEK) surfaces, *Journal of Materials Science: Materials in Medicine* 16(7) (2005) 671-677.
- [57] A. Xu, X. Liu, X. Gao, F. Deng, Y. Deng, S. Wei, Enhancement of osteogenesis on micro/nano-topographical carbon fiber-reinforced polyetheretherketone–nanohydroxyapatite biocomposite, *Materials Science and Engineering: C* 48 (2015) 592-598.
- [58] X. Wu, X. Liu, J. Wei, J. Ma, F. Deng, S. Wei, Nano-TiO<sub>2</sub>/PEEK bioactive composite as a bone substitute material: in vitro and in vivo studies, *International Journal of Nanomedicine* 7 (2012) 1215.

- [59] R.S. Brum, P.R. Monich, F. Berti, M.C. Fredel, L.M. Porto, C.A.M. Benfatti, J.C.M. Souza, On the sulphonated PEEK for implant dentistry: Biological and physicochemical assessment, *Materials Chemistry and Physics* 223 (2019) 542-547.
- [60] M. Fedel, T.T. Wong, G. Speranza, B. Lohberger, M. Nogler, F. Awaja, Hybrid graphene oxide/amorphous carbon coatings and their effect on the viability and toxicity of different cell types, *Surface and Coatings Technology* 374 (2019) 95-102.
- [61] R.A. Surmenev, A review of plasma-assisted methods for calcium phosphate-based coatings fabrication, *Surface and Coatings Technology* 206(8-9) (2012) 2035-2056.
- [62] M.S.A. Bakar, M.H.W. Cheng, S.M. Tang, S.C. Yu, K. Liao, C.T. Tan, K.A. Khor, P. Cheang, Tensile properties, tension–tension fatigue and biological response of polyetheretherketone–hydroxyapatite composites for load-bearing orthopedic implants, *Biomaterials* 24(13) (2003) 2245-2250.
- [63] N. Abbasi, S. Hamlet, R.M. Love, N.-T. Nguyen, Porous scaffolds for bone regeneration, *Journal of Science: Advanced Materials and Devices* 5(1) (2020) 1-9.
- [64] V. Karageorgiou, D. Kaplan, Porosity of 3D biomaterial scaffolds and osteogenesis, *Biomaterials* 26(27) (2005) 5474-5491.
- [65] Y. Su, J. He, N. Jiang, H. Zhang, L. Wang, X. Liu, D. Li, Z. Yin, Additively-manufactured poly-ether-ether-ketone (PEEK) lattice scaffolds with uniform microporous architectures for enhanced cellular response and soft tissue adhesion, *Materials & Design* 191 (2020) 108671.

- [66] H. Spece, T. Yu, A.W. Law, M. Marcolongo, S.M. Kurtz, 3D printed porous PEEK created via fused filament fabrication for osteoconductive orthopaedic surfaces, *Journal of the Mechanical Behavior of Biomedical Materials* 109 (2020) 103850.
- [67] X. Feng, L. Ma, H. Liang, X. Liu, J. Lei, W. Li, K. Wang, Y. Song, B. Wang, G. Li, Osteointegration of 3D-printed fully porous polyetheretherketone scaffolds with different pore sizes, *ACS omega* 5(41) (2020) 26655-26666.
- [68] Z. Liu, M. Zhang, Z. Wang, Y. Wang, W. Dong, W. Ma, S. Zhao, D. Sun, 3D-printed porous PEEK scaffold combined with CSMA/POSS bioactive surface: A strategy for enhancing osseointegration of PEEK implants, *Composites Part B: Engineering* 230 (2022) 109512.
- [69] S.H. Oh, I.K. Park, J.M. Kim, J.H. Lee, In vitro and in vivo characteristics of PCL scaffolds with pore size gradient fabricated by a centrifugation method, *Biomaterials* 28(9) (2007) 1664-1671.
- [70] S. Ishihara, A.J. McEvily, T. Goshima, K. Kanekasu, T. Nara, On fatigue lifetimes and fatigue crack growth behavior of bone cement, *Journal of Materials Science: Materials in Medicine* 11(10) (2000) 661-666.
- [71] I. Maskery, N.T. Aboulkhair, A.O. Aremu, C.J. Tuck, I.A. Ashcroft, Compressive failure modes and energy absorption in additively manufactured double gyroid lattices, *Additive Manufacturing* 16 (2017) 24-29.
- [72] B. Xu, K.-W. Lee, W. Li, M.J. Yaszemski, L. Lu, Y. Yang, S. Wang, A comparative study on cylindrical and spherical models in fabrication of bone tissue engineering scaffolds: Finite element simulation and experiments, *Materials & Design* 211 (2021) 110150.

- [73] M.C. Sobieraj, C.M. Rimnac, Fracture, fatigue, and notch behavior of PEEK, PEEK biomaterials handbook, Elsevier2019, pp. 67-82.
- [74] E.F. Morgan, G.U. Unnikrisnan, A.I. Hussein, Bone mechanical properties in healthy and diseased states, Annual review of biomedical engineering 20 (2018) 119-143.
- [75] F.J.Q. Gonzalez, N. Nuno, Finite element modeling of manufacturing irregularities of porous materials, Biomaterials and Biomechanics in Bioengineering 3(1) (2016) 1-14.
- [76] G. Campoli, M.S. Borleffs, S.A. Yavari, R. Wauthle, H. Weinans, A.A. Zadpoor, Mechanical properties of open-cell metallic biomaterials manufactured using additive manufacturing, Materials & Design 49 (2013) 957-965.
- [77] N. Soro, L. Brassart, Y. Chen, M. Veidt, H. Attar, M.S. Dargusch, Finite element analysis of porous commercially pure titanium for biomedical implant application, Materials Science and Engineering: A 725 (2018) 43-50.
- [78] H. Shen, L.C. Brinson, Finite element modeling of porous titanium, International Journal of Solids and Structures 44(1) (2007) 320-335.
- [79] A. Maiti, W. Small, J.P. Lewicki, T.H. Weisgraber, E.B. Duoss, S.C. Chinn, M.A. Pearson, C.M. Spadaccini, R.S. Maxwell, T.S. Wilson, 3D printed cellular solid outperforms traditional stochastic foam in long-term mechanical response, Scientific reports 6(1) (2016) 1-9.
- [80] Q. Li, W. Zhao, Y. Li, W. Yang, G. Wang, Flexural properties and fracture behavior of CF/PEEK in orthogonal building orientation by FDM: Microstructure and mechanism, Polymers 11(4) (2019) 656.



- [81] P. Sikder, Y. Ren, S.B. Bhaduri, Microwave processing of calcium phosphate and magnesium phosphate based orthopedic bioceramics: A state-of-the-art review, *Acta Biomaterialia* 111 (2020) 29-53.
- [82] P. Sikder, N. Koju, Y. Ren, V.K. Goel, T. Phares, B. Lin, S.B. Bhaduri, Development of single-phase silver-doped antibacterial CDHA coatings on Ti6Al4V with sustained release, *Surface and Coatings Technology* 342 (2018) 105-116.
- [83] P. Sikder, S.B. Bhaduri, J.L. Ong, T. Guda, Silver (Ag) doped magnesium phosphate microplatelets as next-generation antibacterial orthopedic biomaterials, *Journal of Biomedical Materials Research Part B: Applied Biomaterials* 108(3) (2020) 976-989.

### **Chapter III**

- [1] Ginebra, Maria-Pau, Tania Traykova, and Josep A. Planell. "Calcium phosphate cements as bone drug delivery systems: a review." *Journal of controlled release* 113.2 (2006): 102-110.
- [2] Lamon, Jacques, and Narottam P. Bansal. *Ceramic Matrix Composites: Materials, Modeling and Technology*. John Wiley & Sons, 2014.
- [3] Holkar, Chandrakant R., et al. "Scale-up technologies for advanced nanomaterials for green energy: feasibilities and challenges." *Nanomaterials for Green Energy*. Elsevier, 2018. 433-455.
- [4] Geim, Andre Konstantin. "Graphene: status and prospects." *science* 324.5934 (2009): 1530-1534.

- [5] Golzar, Hossein, et al. "Incorporation of functionalized reduced graphene oxide/magnesium nanohybrid to enhance the osteoinductivity capability of 3D printed calcium phosphate-based scaffolds." *Composites Part B: Engineering* 185 (2020): 107749.
- [6] Subramaniaswamy, V., et al. "An ontology-driven personalized food recommendation in IoT-based healthcare system." *The Journal of Supercomputing* 75.6 (2019): 3184-3216.